Global stability analyses of Mack mode on the windward face of a hypersonic yawed cone

Xi Chen ⬤, Siwei Dong, Guohua Tu, Xianxu Yuan,[*] and Jianqiang Chen[†]
State Key Laboratory of Aerodynamics, China Aerodynamics Research and Development Center,
Mianyang 621000, China

Steady laminar flow over a blunt cone at $5°$ angle of attack has been computed at Mach number 6 and unit Reynolds number $Re_\infty^* = 2.079 \times 10^7 \ m^{-1}$. The flow conditions are selected to match the flight test conducted by China Aerodynamics Research and Development Center at an altitude of 16 km where windward-side boundary-layer transition was detected. In order to understand the underlying transition mechanisms, we perform local and global stability analyses, focusing on linear and nonlinear stability characteristics of Mack-mode instability which prevails in the windward side. The global instability spectrum contains two distinct types of modes: few isolated eigenmodes (branch D) lying in the vicinity of the windward ray, and an arc branch (branch S) of eigenmodes in the outboard region. D modes originate in branch S and are considerably more unstable than S modes, potentially causing an indented transition front. Nonlinear development of a single symmetric D mode that inherently contains broadband oblique components will inevitably trigger the fundamental resonance without additional perturbations, once the mode temperature amplitude exceeds 10% of the free-stream value; moreover, the combination resonance is subordinate to the fundamental resonance as the latter always occurs prior to the former. The antisymmetric D mode is less amplified than the symmetric counterpart, yet it is still able to rapidly broaden the azimuthal wave-number spectrum through triad interactions among oblique components. In either case, the global primary mode is found to act as a catalyst to promote rapid amplifications of certain oblique components that ultimately lead to streaky structures in the vicinity of the windward ray. The streaks in turn are significantly unstable to low-frequency waves that are likely responsible for the final breakdown.

I. INTRODUCTION

Boundary-layer transition is of great importance in vehicle designs, but has not yet been fully understood. Since the pioneering work of Lees and Lin [1], stability of compressible boundary layers has been extensively studied. For flows at low and moderate Mach numbers, the first Mack mode with a wave angle of around $60°$ is dominant. For hypersonic flows, the second Mack mode (abbreviated as Mack mode hereafter) is generally more unstable [2]. Mack mode is dominated by the planar component for two-dimensional boundary layers, while its oblique counterpart prevails in three-dimensional configurations [3]. The circular-base cone exposed at a nonzero angles of attack (AoA) to oncoming hypersonic flows is a frequently used model to understand three-dimensional boundary-layer transition. In this configuration, the azimuthal pressure gradient drives the fluid from

---

[*]yuanxianxu@cardc.cn
[†]chenjq@cardc.cn

the windward ray towards the leeward ray where low-momentum fluid is lifted up forming large-scale streamwise vortices. Of particular interest is the boundary-layer instability in the windward side where main heating happens and therefore it is most critical for the performance of the high-speed vehicle.

Stability characteristics of the windward boundary layer were addressed mostly via one-dimensional linear stability theories (LST and PSE2D) [4–8]. The previous results confirm coexistence of the crossflow instability and the Mack-mode instability. One-dimensional stability methodology assumes that eigenfunctions of instability modes are uniform (two dimensional) or periodic in the azimuthal direction, which is not strictly valid in the windward side since the boundary layer varies azimuthally. Relaxing the azimuthal homogeneity assumption, Paredes *et al.* [9] adopted the BiGlobal approach to analyze the windward boundary layer of a hypersonic yawed sharp cone under a typical wind-tunnel condition (with a nearly adiabatic wall condition). They found a planar Mack mode peaking on the windward ray and oblique Mack modes peaking at a certain distance from the windward ray. Nevertheless, the windward boundary-layer instability is still unclear regarding the global eigenvalue spectrum and the streamwise evolution of global modes.

When the Mack-mode amplitude grows to exceed a certain threshold (say 1% of free-stream velocity), nonlinear interactions set in. As a result, the mean flow is distorted, harmonics emerge, and other types of disturbances may be heavily amplified owing to parametric instabilities. For an axisymmetric cone boundary layer under typical hypersonic wind-tunnel conditions, K-type or fundamental breakdown [10,11] is demonstrated to be one of the dominant transition paths (see, for example, [12,13], and works of Fasel's group [14] and references therein). In this path, a planar Mack mode, a pair of oblique modes at the same frequency as the Mack mode, and a streamwise-vortex mode compose a fundamental resonance, resulting in longitudinal streaks in the flow field. Moreover, combination resonance of a planar Mack mode, an (a pair of) oblique mode(s) with different but close frequencies as the planar mode, and the difference and sum modes nonlinearly generated by the former two, is an important spectral-broadening mechanism complementing the fundamental resonance. In both types of resonances, the planar Mack mode plays a catalytic role in promoting secondary modes [13]. In contrast, secondary instability computations conducted by Li *et al.* [15] for one time instant during the ascent phase of the HIFiRE-1 flight test indicate that the subharmonic resonance comprising of a planar Mack mode and a pair of subharmonic oblique waves (with half-frequency of the Mack mode) is stronger than the fundamental resonance. However, as far as the authors are concerned, secondary instability mechanisms of Mack modes have until now only been identified for axisymmetric configurations. Whether they are still active in an essentially three-dimensional boundary layer especially under a flight condition and, if so, which one is dominant, are still unknown.

Oblique breakdown initiated by a pair of oblique waves (first mode, second modes, or entropy disturbances) with equal but opposite wave angles is another relevant nonlinear transition mechanism for axisymmetric conical boundary layers [16,17]. The primary oblique waves generate a steady mode with twice the spanwise wave number as the primary oblique wave [18]. The steady mode then undergoes a transient growth process [19] and a subsequent exponential growth stage, eventually becoming the dominant component preceding the transition. In the presence of crossflow, the boundary layer prefers to instability waves with either positive or negative wave angles but not both (see, for example, [20]). As a consequence, oblique breakdown can hardly be triggered in the crossflow regions of three-dimensional configurations. Nonetheless, it is interesting to assess whether oblique breakdown is relevant in the vicinity of symmetry planes (windward or leeward ray) where crossflow is expected to be week. Experimental investigations into the windward boundary-layer transition have been undertaken by many investigators, focusing on the parametric variations of the transition front (see [22] for a comprehensive summary). For most cases, transition first occurs along the leeward ray, and last appears along the windward ray, forming a V-like transition front (see also [23] for further details). In contrast, an indented (W-like) transition front was detected during the reentry phase of HIFiRE-1 flight test, that is, the maximum transition Reynolds number
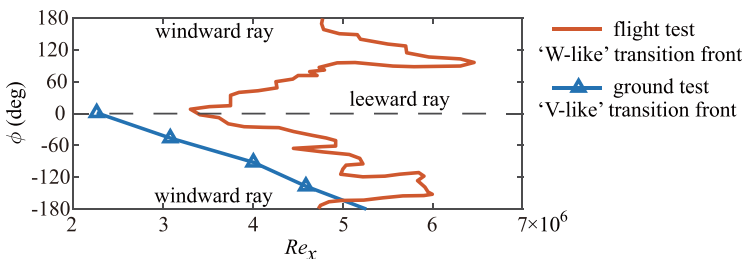
FIG. 1. Qualitative comparison between the transition front measured in a ground test and that detected in the HIFiRE-1 flight test for the HIFiRE-1 cone model at nonzero angle of attacks. Figure adapted from Stanfield *et al.* [21].

occurs about $30°$ to $80°$ away from the windward ray at moderate AoAs [21] as illustrated in Fig. 1. The hypersonic flight test of a cone model carried out by China Aerodynamics Research and Development Center (CARDC) also showed that the windward boundary-layer transition first occurs in the vicinity of the windward ray rather than in the outboard region [24]. Similar observations were also documented in several ground tests (e.g., [25,26]). Since these ground tests and the flight tests were all conducted at low wall-to-adiabatic wall temperature ratios (below 0.3), it is natural to speculate that the cold wall conditions may promote the windward transition through enhancing the Mack-mode instability.

Because of much thinner boundary-layer thicknesses in the windward side and thus substantially higher Mack-mode instability frequencies (generally larger than 500 kHz) than those of the axisymmetric conical configurations under the same flow condition, quantitative experimental measurements are very difficult. Likewise, such a high frequency corresponds to an extremely small streamwise scale that requires prohibitive mesh sizes in numerical simulations. The first computational work regarding the windward transition triggered by Mack-mode waves comes from Yang [27]. Considering a trajectory point of the flight test conducted by CARDC, Yang carried out direct numerical simulations modeling the nonlinear development of single-frequency Mack-mode waves excited by azimuthally uniform blowing and suction. They found that the Mack-mode waves propagating downstream are eventually confined in the vicinity of the windward ray. Later, Yang *et al.* [28] simulated the spatial evolution of a nonlinear wave packet initiated by a short-duration pulse on the windward ray. The wave packet features quasi-two-dimensional Mack-mode waves and the ensuing streaky structures, favoring the fundamental breakdown scenario. However, albeit with a total of 1.55×10^{11} grid points in the simulation, the transitional flow field was still underresolved, especially in the azimuthal direction.

An alternative approach to investigate the windward boundary-layer transition is to use the nonlinear parabolized stability equations (NPSE). The line-marching NPSE (NPSE2D) developed by Bertolotti *et al.* [29] track the nonlinear development of disturbances along a line and have been successfully applied in many essentially two-dimensional configurations [30]. The plane-marching counterpart (NPSE3D), accounting for the azimuthal inhomogeneity of the base flow, was shown to adequately predict the nonlinear evolution of the global modes in trailing vortices and (two-dimensional) boundary layers [31,32]. Furthermore, the ability of PSE to probe effects of each term of disturbance equation in isolation or in a combined manner can yield tremendous physical insight into the transition dynamics. For instance, one can easily isolate the energy transfer pertaining to linear operators from that associated with nonlinear terms.

In this paper, we attempt to investigate the Mack-mode instability on the windward surface of a hypersonic yawed cone at nominally the same flow condition as used in Yang [27] via NPSE as well as other stability analysis tools. As aforementioned above, previous theoretical studies on such a configuration mostly considered local linear stability characteristics; little is known about the global instability behaviors and nonlinear instability mechanisms. The aim of this study is thus twofold:

first to fully reveal linear stability characteristics of Mack mode from the global point of view, and second to understand how the Mack mode breaks down in a truly three-dimensional boundary layer under a typical flight condition. This paper is organized as follows. The adopted numerical setup and stability theories are introduced in Sec. II; linear and nonlinear stability analyses are carried out in Sec. III; and finally, a summary and conclusions are offered in Sec. IV.

II. NUMERICAL SETUP AND STABILITY THEORIES

The numerical simulation and stability analysis are based on the equations of ideal gas flow written in dimensionless form as

$$\frac{\partial \rho}{\partial t} + \nabla \cdot (\rho V) = 0, \tag{1}$$

$$\rho \left[\frac{\partial V}{\partial t} + (V \cdot \nabla) V \right] = -\nabla P + \frac{1}{\mathrm{Re}} \nabla \cdot \left[\mu \left(\nabla V + \nabla V^t - \frac{2}{3} \nabla \cdot V \mathbf{I} \right) \right], \tag{2}$$

$$\rho \left[\frac{\partial T}{\partial t} + (V \cdot \nabla) T \right] = (\gamma - 1) \mathrm{Ma}^2 \left[\frac{\partial P}{\partial t} + (V \cdot \nabla) P \right] + \frac{1}{\mathrm{Re\,Pr}} \nabla \cdot (\kappa \nabla T)$$
$$+ \frac{(\gamma - 1) \mathrm{Ma}^2 \mu}{2 \mathrm{Re}} \left(\nabla V + \nabla V^t - \frac{2}{3} \nabla \cdot V \mathbf{I} \right) : \left(\nabla V + \nabla V^t - \frac{2}{3} \nabla \cdot V \mathbf{I} \right), \tag{3}$$

where $V = (U, V, W)$ is the velocity vector, $\mathbf{I}$ the identity tensor, ρ the density, P the pressure, T the temperature, Ma the Mach number, Re the Reynolds number, $\mathrm{Pr} = 0.7$ the Prandtl number, $\gamma = 1.4$ the specific-heat coefficient, κ the thermal conductivity, μ the first coefficient of viscosity. The reference values of velocity and temperature are the corresponding values at the free stream with the subscript $(\cdot)_\infty$. The reference value for pressure is $\rho_\infty U_\infty^2$. The equation of state is $p = \rho T / (\gamma M^2)$. The Stokes's law has been assumed and the viscosity coefficient is estimated by Sutherland's law

$$\mu = T^{3/2} \frac{1 + Cs}{T + Cs} \tag{4}$$

with $Cs = 110.4 \, \mathrm{K} / T_\infty^*$ for air in standard conditions. The dimensional variables are denoted with the superscript $(\cdot)^*$.

A. Flow configuration

The model currently being studied is a $7°$ half-angle blunt cone at $5°$ angle of attack. The model is 900 mm long and has a nose radius of 5 mm. Flow conditions correspond to a Mach 6 flow at an altitude of 16.0 km, that is, unit Reynolds number $\mathrm{Re}_\infty^* = 2.079 \times 10^7 \, \mathrm{m}^{-1}$, free-stream static temperature $T_\infty^* = 216 \, \mathrm{K}$, and total temperature $T_0^* = 1786 \, \mathrm{K}$. A wall boundary condition of $T_w^* = 500 \, \mathrm{K}$ is also imposed, leading to the wall temperature ratio $T_w^* / T_0^* = 0.28$. This wall temperature is representative as measured in flight tests of conic models [7,33]. Although the wall temperatures in the vicinity of the nose tip region are expected to be considerably higher in realistic flights, adopting a constant value is a good approximation to the surface temperature downstream of the nose [7,33]. Moreover, the wall-temperature differences in the nose region are shown to have little effects on boundary-layer stability [15,34]. The detailed flow configuration can be found in Fig. 2. All flow quantities are nondimensionalized using the arbitrarily prescribed reference length $L^* = 0.0537 \, \mathrm{mm}$ (the boundary-layer scale at $X^* = 60 \, \mathrm{mm}$), the free-stream velocity, density, and temperature.

B. Base flow calculations

The well-tested parallel computational fluid dynamics software OPENCFD, developed by Li *et al.* [35], was used for the base flow calculations. The computations employ a hybrid strategy
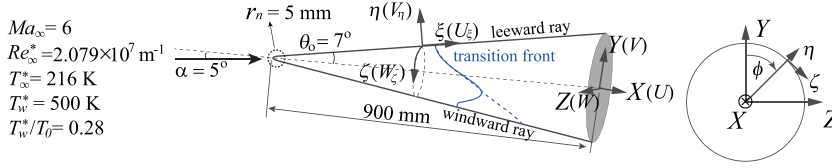
FIG. 2. Sketch of the flow configuration, laboratory, and body-oriented coordinates, and the conventional (indented) transition front [blue dashed (solid) line]. The velocity components in the laboratory coordinates (U, V, W) and in the body-oriented coordinates (U_ξ, V_η, W_ζ) are also shown.

similar to that used by Fasel's group (see, for example, [36,37]) and by Li *et al.* [38] in studying hypersonic boundary-layer transition problems. This strategy includes two steps. First, the entire flow field is computed using the finite-volume algorithm with a second-order accurate scheme. The grid size is $N_\xi \times N_\eta \times N_\zeta = 1000 \times 401 \times 181$, where N_ξ, N_η, N_ζ are the number of grid points in the streamwise, wall-normal, and azimuthal direction, respectively. Then, the calculated steady flow serves as inlet conditions for the high-order finite-difference calculation which is performed for a smaller computational domain downstream of the nose tip ($X^* \in [45\,900]$ mm). The inviscid fluxes are computed by using a seventh-order upwind finite-difference scheme, while the viscous fluxes are discretized using a sixth-order central-difference scheme. The time integration is performed using a third-order Runge-Kutta scheme. The grid size is $N_\xi \times N_\eta \times N_\zeta = 600 \times 400 \times 500$, with the grid distribution being illustrated in Figs. 3(a) and 3(b). The grid points in the streamwise direction are uniformly distributed before $X^* = 650$ mm, followed by a buffer region where the grid spacings are gradually increased towards the outlet. In the wall-normal direction, the grid is stretched so that sufficient (at least 100) points are within the boundary layer, and is furthermore aligned with the leading-edge shock to diminish the numerical oscillations from the shock layer. Thanks to the azimuthal symmetry, only half part of the flow field is simulated. The grid points are equally spaced for the windward side, while a total of 200 points are put in $\phi \in [0, 45]^\circ$ of the leeward side where streamwise vortices are expected to be present. Compared with previous DNS studies [9,39], this grid resolution is sufficient for the purpose of the base flow calculation. The overall character of the base flow is illustrated in Fig. 3(c). The angle of attack produces spanwise pressure gradients, which induce cross flow in the cone side and a liftup of the low-momentum boundary-layer fluid at the leeward ray, generating a large-scale mushroom structure. Circumferential variation of streamwise, crossflow, and wall-normal velocity profiles at $X^* = 400$ mm is shown in Figs. 4(a)–4(c), respectively. Away from the windward ray ($\phi = 180^\circ$), the boundary-layer thickness increases
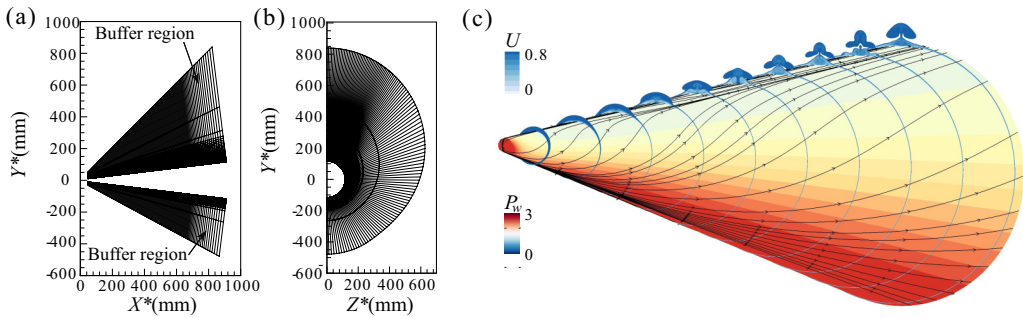

FIG. 3. Sketch of the grid distribution for the finite-difference calculation and of the flow field: (a) X^*-Y^* plane, (b) Z^*-Y^* plane. In (a) and (b), every fifth point in the streamwise direction and every fourth point in other two directions are shown. (c) Contours of wall pressure (P_w) and axial velocity (U) at several axial locations from $X^* = 45$ mm to $X^* = 650$ mm, with surface streamlines.
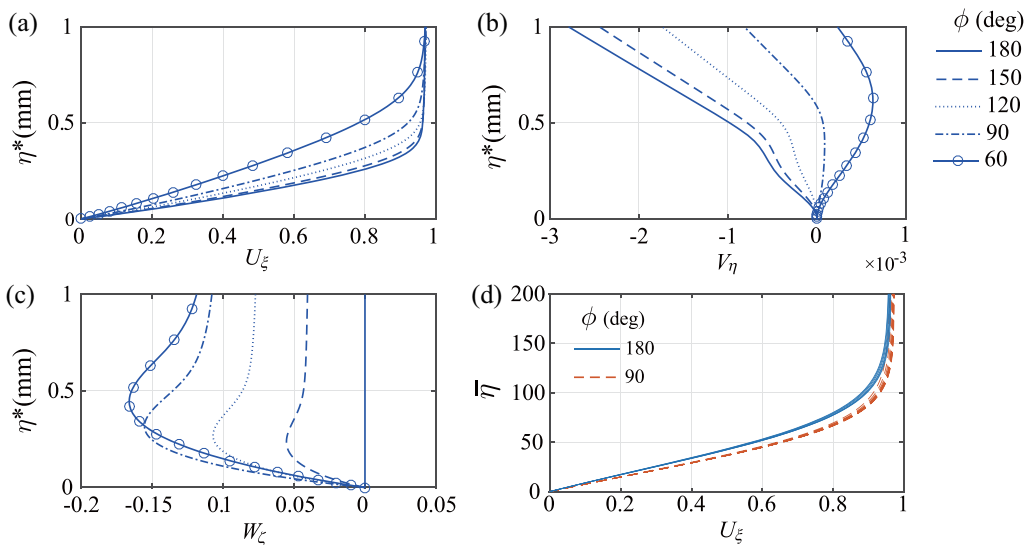
FIG. 4. Azimuthal variations ($\phi : 180° \mapsto 60°$) of the base flow profiles at $X^* = 400$ mm. (a) Streamwise velocity U_ξ; (b) wall-normal velocity V_η; (c) crossflow velocity W_ζ; (d) self-similarity in the streamwise direction for the streamwise velocity at the windward ray and the side line for 350 mm $< X^* <$ 700 mm with the similarity variable $\bar{\eta} \equiv \sqrt{3/2\, \mathrm{Re}_\infty^*/X^*} \int_0^{\eta^*} \bar{\rho}\, d\eta^*$ [40].

continuously, the wall-normal velocity profile turns from negative to positive when entering the leeward side, and the peak crossflow velocity increases from 0 to beyond 15% free-stream velocity. As shown in Fig. 4(d), the self-similarity of the streamwise velocity profiles within the boundary layer is evident along the windward ray for $X^* > 350$ mm, like the observation by Li *et al.* [4] in the investigation of HIFiRE-1 configuration, and is still visible in the side region. This implies that the entropy layer effects are negligibly small in the region of interest which is far downstream of the nose region.

C. Stability theories

Below we will give a brief introduction to the formulations of different theoretical tools utilized in this study, as summarized in Table I. Owing to the complexity of this problem, i.e., the inherent three dimensionality of this configuration and the potential nonlinearity that is completely unknown yet, we attempt to march steadily from a local to global perspective and at the same time from

TABLE I. Theoretical tools utilized in this study. The computational cost generally increases from top to bottom.

Tools	Linear/nonlinear	Local/global	Roles
LST	Linear	Local	Quickly assess the primary instabilities
NPSE2D	Nonlinear	Local	Explore the potential
Floquet analysis			Mode resonance mechanisms
BiGlobal	Linear	Global	Reveal the linear global stability
LPSE3D			features and the streak instabilities
NPSE3D	Nonlinear	Global	Study the nonlinear development and
			breakdown process of global modes

linear to nonlinear instabilities. Therefore, multiple theoretical tools were utilized in this study. Based on the laminar base flow obtained by the direct numerical simulation, we first employ LST to sketch the primary instabilities in the windward side of the blunt cone in an intuitive way, then use BiGlobal and PSE3D to study the linear global stability characteristics for representative frequencies at several axial stations, determining the most dangerous modes that likely trigger the transition. The nonlinear development of these dangerous modes and potential mode resonance mechanisms are then investigated in detail via local (one-dimensional) nonlinear stability theories (NPSE2D and Floquet theory) first, if possible, and then the global nonlinear analysis (NPSE3D). The rationale is that the existing frameworks of nonlinear transition mechanisms [10,11,18] are almost entirely established based on local approaches, and the local stability analysis results along a representative ray initiated from the nose tip of the blunt cone are supposed to shed light on the nonlinear transition mechanisms in such a truly three-dimensional configuration. Different theoretical methods focus on different aspects of this problem and are coupled in some ways. For instance, BiGlobal provides the initial profiles for the PSE3D marching. Moreover, comparison among results of different tools is made when possible to achieve a comprehensive description of transition mechanisms and more convincing conclusions.

1. LST

In the formulation of one-dimensional linear stability theory (LST), the boundary layer is assumed to be parallel in the streamwise direction (i.e., the boundary-layer thickness does not change) and uniform in the azimuthal direction. The flow field can thus be decomposed as

$$\boldsymbol{q}(\xi, \eta, \zeta, t) = \bar{\boldsymbol{q}} + \boldsymbol{q}' = \bar{\boldsymbol{q}}(\eta) + \hat{\boldsymbol{q}}(\eta) \exp(i\alpha\xi - in\phi - i\omega t) + \text{c.c.}, \tag{5}$$

where $\boldsymbol{q} \equiv (U, V, P, T, W)^{tr}$, $\bar{\boldsymbol{q}}$ denotes the basic states, $\boldsymbol{q}'$ the perturbations, $\hat{\boldsymbol{q}}$ the shape function of the disturbances, c.c. the complex conjugate. (U, V, W) is the velocity vector, P is the pressure, and T is the temperature. The streamwise and azimuthal coordinates ξ and ζ only act as parameters in the base flow profiles. α represents the streamwise wave number, with the imaginary part giving the growth rate. n is an integer denoting the azimuthal wave number around the conic surface. The local wave angle Ψ is defined as $\Psi \equiv \arctan[n/\alpha r(\xi)]$, $r(\xi)$ the local radius of the cone. ω is the angular frequency with the corresponding dimensional frequency denoted by f^*. After substituting the above decompositions into the Navier-Stokes equations, subtracting the basic states and neglecting the nonparallel and nonlinear terms, one obtains a nonlinear eigenvalue problem about α, which is iteratively solved with help of Malik's compact finite-difference scheme [41]. Note that effects of the azimuthal curvature and body divergence have been considered in LST.

2. BiGlobal

From the global point of view, the base flow is not necessarily uniform in the azimuthal direction, and the perturbations can be written in a form as

$$\boldsymbol{q}'(\xi, \eta, \zeta, t) = \hat{\boldsymbol{q}}(\eta, \zeta) \exp(i\alpha\xi - i\omega t) + \text{c.c.}, \tag{6}$$

which also leads to a nonlinear eigenvalue problem. By introducing an auxiliary vector $\tilde{\boldsymbol{q}} = [\hat{\boldsymbol{q}}; \alpha\hat{\boldsymbol{q}}]$, the nonlinear eigenvalue problem becomes a linear two-dimensional eigenvalue problem (BiGlobal) as

$$\mathcal{A}\tilde{\boldsymbol{q}} = \alpha\mathcal{B}\tilde{\boldsymbol{q}}. \tag{7}$$

The entries of the matrix operators $\mathcal{A}$ and $\mathcal{B}$ can be found in Chen *et al.* [20]. The calculation domain covers half the cone surface, i.e., $\phi \in [0, 180]°$. Symmetry or antisymmetry boundary conditions are implemented at the windward ray ($\phi = 180°$) according to the mode symmetry, while Dirichlet boundary conditions are forced for all the variables except for pressure at wall and infinity as well as at the leeward ray ($\phi = 0°$). A sixth- and an eighth-order FD-q scheme [42] are used to discretize the azimuthal and wall-normal direction, respectively. The eigenvalues are then determined by using

Arnoldi's method. Unless otherwise stated, the BiGlobal modes are resolved by 601 points in the azimuthal direction and 101 points in the wall-normal direction. In particular, the azimuthal grid is stretched so that each wavelength in the core region of an investigated mode contains at least 20 points. Such a grid system proves to accurately capture the global modes, as shown in Appendix B.

3. NPSE2D and NPSE3D

In order to relax the parallel-flow assumption made by the theories above (LST and BiGlobal), one can parabolize the stability equations by assuming the flow quantities to be "weakly varying" in the streamwise direction. This modifies LST and BiGlobal equations to the line-marching parabolized stability equations (PSE2D) and the plane-marching parabolized stability equations (PSE3D), respectively.

In the formulation of PSE2D, the disturbance is decomposed into a rapidly varying wavelike part and a slowly varying shape function as follows:

$$\boldsymbol{q}'(\xi, \eta, \zeta, t) = \sum_{m,n} \hat{\boldsymbol{q}}_{mn}(\xi, \eta) \exp \left(i \int_0^\xi \alpha_{mn} d\xi - in\phi - i\omega_m t \right) + \text{c.c.}, \tag{8}$$

where ω_0 is the primary frequency; $\hat{\boldsymbol{q}}_{mn}$ is the shape function for the Fourier mode (m, n); and α_{mn} and ω_m are, respectively, the associated streamwise (complex) wave number and frequency. The shape function is assumed to be a slowly varying function of the streamwise coordinate so that its second derivative with respect to ξ is negligible. Substitute Eq. (8) into the Navier-Stokes equations and subtract the mean-flow equation to obtain the governing equations for the shape functions of each mode (m, n) as

$$\mathcal{L}_{mn}\hat{\boldsymbol{q}}_{mn} + \mathcal{M}_{mn}\frac{\partial \hat{\boldsymbol{q}}_{mn}}{\partial \xi} = \mathcal{F}_{mn}, \tag{9}$$

where $\mathcal{L}_{mn}$ and $\mathcal{M}_{mn}$ are linear operators discretized by the same schemes as used in LST, and their entries can be found in Zhu *et al.* [43]. $\mathcal{F}_{mn}$ are the nonlinear forcings contributed by other modes. This system of equations is parabolic and thus requires boundary and initial conditions. The initial conditions are provided by the LST results. The boundary conditions read as

$$\hat{U}_{mn}, \hat{V}_{mn}, \hat{T}_{mn}, \hat{W}_{mn} = 0 \quad \text{at} \quad \eta = 0 \quad \text{and} \quad \infty, \tag{10}$$

which correspond to no-slip and no-temperature-fluctuation boundary conditions at the wall, and vanishing temperature and velocity disturbances as $\eta \to \infty$. The boundary conditions for density amplitude function are implicitly fulfilled by the continuity equation at the boundaries. However, for the mean-flow distortion $(0,0)$, the infinity condition for the wall-normal velocity is replaced by

$$\frac{\partial \hat{V}_{00}}{\partial \eta} = 0 \quad \text{at} \quad \eta = \infty, \tag{11}$$

which accounts for the boundary-layer growth. Equations (9) are marched forward using the first-order Euler backward scheme. The Vigneron technique is used to avoid instabilities caused by the residual ellipticity [18]. To avoid the ambiguity in the ξ dependence between $\hat{q}$ and α, a normalized condition is used:

$$\int_\eta \frac{\bar{T}}{\gamma M^2 \bar{\rho}} \hat{\rho}^\dagger \frac{\partial \hat{\rho}}{\partial \xi} + \bar{\rho} \left(\hat{U}^\dagger \frac{\partial \hat{U}}{\partial \xi} + \hat{V}^\dagger \frac{\partial \hat{V}}{\partial \xi} + \hat{W}^\dagger \frac{\partial \hat{W}}{\partial \xi} \right) + \frac{\bar{\rho}\hat{T}^\dagger \partial \hat{T}/\partial \xi}{\gamma(\gamma-1)M^2\bar{T}} d\eta = 0, \tag{12}$$

where the $\dagger$ symbol denotes the complex conjugate.

Similarly, in the PSE3D formulation, the infinitesimal perturbation takes the form [31]

$$\boldsymbol{q}'(\xi, \eta, \zeta, t) = \sum_m \hat{\boldsymbol{q}}_m(\xi, \eta, \zeta) \exp \left(i \int_\xi \alpha_m(\xi) d\xi - i\omega_m t \right) + \text{c.c.}, \tag{13}$$

where $\partial^2 \hat{\boldsymbol{q}}_m / \partial \xi^2 \ll 1$. The governing equations for each component read as

$$\mathcal{L}_m \hat{\boldsymbol{q}}_m + \mathcal{M}_m \frac{\partial \hat{\boldsymbol{q}}_m}{\partial \xi} = \mathcal{F}_m, \tag{14}$$

where $\mathcal{L}_m$ and $\mathcal{M}_m$ are linear operators discretized by the same schemes as used in BiGlobal, and their entries can be found in Chen *et al.* [20]. $\mathcal{F}_m$ denote the nonlinear terms contributed by other components. With the initial profiles provided by BiGlobal, the streamwise evolution of perturbations is adequately resolved using the first-order backward Euler method. Similar boundary and normalized conditions with PSE2D are used. The NPSE3D code is verified against the NPSE2D results for a two-dimensional configuration (see Appendix A).

When neglecting the right-hand-side nonlinear terms, PSE reduce to linear equations. Hereafter, the linear and nonlinear forms of PSE are referred to LPSE and NPSE, respectively.

4. Floquet analysis

In the context of one-dimensional stability analysis, Floquet theory is well known to be able to adequately describe the behaviors of the secondary instabilities in the parametric-resonance stage [10,13,44]. In the parametric-resonance stage, the base flow $\bar{\boldsymbol{q}}_p$ at one streamwise location is the undisturbed laminar flow plus Mack mode, the mean flow distortion (MFD), and the harmonics as

$$\bar{\boldsymbol{q}}_p = \bar{\boldsymbol{q}}(\eta) + \hat{\boldsymbol{q}}_{\text{Mack}}(\eta) \exp(i\alpha\xi - i\omega t) + \hat{\boldsymbol{q}}_{\text{MFD}}(\eta) + \text{harmonics} + \text{c.c.} \tag{15}$$

According to Floquet theory [10], the quasiperiodic base flow given by Eq, (15) can support three-dimensional disturbances for a given azimuthal wave number n as follows:

$$\hat{\boldsymbol{q}}_s = \exp[\gamma\xi - in\phi + \sigma_d(i\alpha\xi - i\omega t)] \sum_{m=-\infty}^{\infty} \hat{\boldsymbol{q}}_m(\eta) \exp[m(i\alpha\xi - i\omega t)] + \text{c.c.,} \tag{16}$$

where γ is the characteristic exponent with its real part denoting the growth rate; σ_d is a detuning parameter that distinguishes the various types of secondary instabilities. The fundamental resonance corresponds to $\sigma_d = 0$. The subharmonic resonance is associated with the case of $\sigma_d = 0.5$. For $0 < \sigma_d < 0.5$, the secondary waves are called combination resonance modes (or detuned modes). Since amplitude of $\hat{q}_m$ generally decays rapidly with m, practical calculations usually need to retain three terms in the solution as

$$\hat{\boldsymbol{q}}_s = e^{\gamma\xi - in\phi + \sigma_d(i\alpha\xi - i\omega t)}(\hat{\boldsymbol{q}}_{-1}(\eta)e^{-(i\alpha\xi - i\omega t)} + \hat{\boldsymbol{q}}_0(\eta) + \hat{\boldsymbol{q}}_1(\eta)e^{i\alpha\xi - i\omega t}) + \text{c.c.} \tag{17}$$

In the fundamental resonance case ($\sigma_d = 0$), the first and third terms of Eq. (17) are referred to as oblique fundamental modes, and the second term is the streamwise-vortex (or difference) mode. In the combination resonance case ($0 < \sigma_d < 0.5$), these three terms are referred to as the side-band, difference, and sum modes, respectively. For the sake of simplicity, we refer to the side-band, difference, and sum modes as combination modes when they are discussed as a whole.

Substituting Eqs. (15) and (17) into the Navier-Stokes equations, neglecting the nonparallel effects and the high-order terms of the disturbances, yield an eigenvalue problem of the form

$$\mathcal{H}[\hat{\boldsymbol{q}}_{-1}, \hat{\boldsymbol{q}}_0, \hat{\boldsymbol{q}}_1]^{\text{tr}} = 0, \tag{18}$$

where $\mathcal{H}$ is a function of the base flow and the wave parameters including the eigenvalues; tr stands for the transpose. This equation along with the same boundary conditions as LST is solved using the same numerical methods as for the LST problem.

The codes for the stability analyses above have been well verified against direct numerical simulation (DNS) results and well validated by experimental results in previous studies [13,20,45–47].
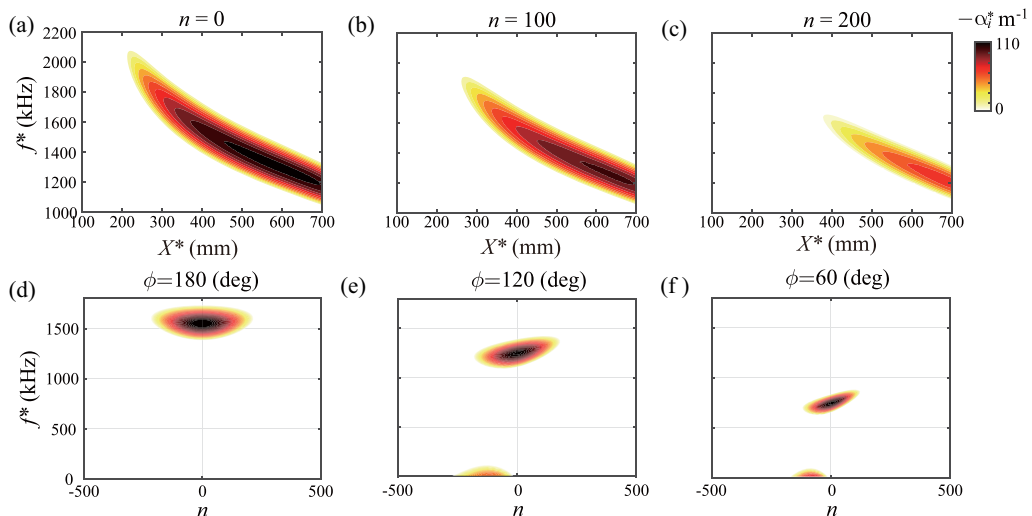
FIG. 5. Contours of the constant amplification rate $-\alpha_i$ from LST: (a)–(c) in the X^*-f^* plane at the windward ray ($\phi = 180°$) with various azimuthal wave numbers n; (d)–(f) in the n-f^* plane at $X^* = 400$ mm for various azimuthal locations.

III. RESULTS AND DISCUSSIONS

A. Local primary instabilities

Before proceeding to multidimensional analyses, we first present LST results that provide us a whole picture on the stability characteristics. Figures 5(a)–5(c) display the distribution of growth rates of Mack mode in the X^*-f^* plane at the windward ray. It can be seen that the Mack-mode instability emerges in an extremely high-frequency region, whose peak frequency progressively decreases from about 2 MHz at $X^* \approx 200$ mm to about 1.2 MHz at $X^* = 700$ mm. Furthermore, the Mack-mode instability is notably stabilized as the azimuthal wave number increases from 0 to 200, indicating that planar components are more unstable than the oblique ones. Figures 5(d)–5(f) shows stability diagrams of high-frequency Mack modes and low-frequency crossflow modes at various azimuthal locations of $X^* = 400$ mm. In the outboard region, the crossflow is present, inducing crossflow instabilities. Away from the windward ray, the Mack-mode instability slowly diminishes with peak frequencies decreasing, whereas the crossflow instability is slightly enhanced as the crossflow velocity strengthens. In the presence of crossflow, the Mack-mode unstable region becomes asymmetric with respect to the azimuthal wave number. Nevertheless, the most unstable component remains essentially two dimensional. Since the Mack-mode instability is dominant in the windward surface, we hereafter focus on it.

B. Global stability characteristics of Mack mode

Albeit neglecting the azimuthal inhomogeneity of base flow, the LST results above serve as a good reference in searching the global unstable modes. Since the leading dimensions of the matrices involved in (spatial) BiGlobal are several orders of magnitude larger than when solving LST [48], it is nearly impossible to obtain global stability diagrams like Fig. 5. Rather, we attempt to inspect the global stability characteristics of certain frequencies at several axial locations, and furthermore to find the most unstable mode.
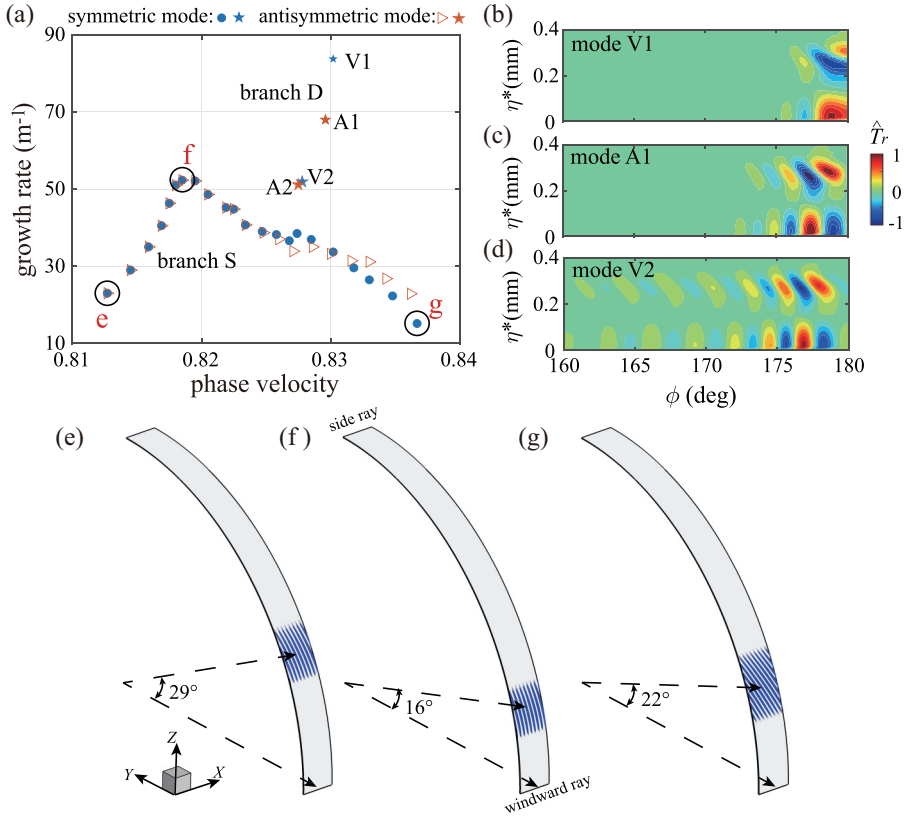
FIG. 6. (a) Global eigenvalue spectra of the Mack-mode instability for frequency 1650 kHz at $X^* = 400$ mm, with real part of the normalized temperature eigenfunctions of first three leading D modes being displayed in (b)–(d). (e)–(g) The spatial structures (including eight axial wavelengths) of three representative S modes [marked by characters in (a)] are illustrated by isosurfaces of real part of normalized temperature eigenfunction $\mathrm{Re}[\hat{T}(\eta, \zeta) \exp(i\alpha\xi)]$, with value of 0.5.

1. Global eigenvalue spectrum and shape functions

A representative global eigenvalue spectrum is displayed in Fig. 6(a) for a frequency of 1650 kHz at $X^* = 400$ mm. Contrary to the conventional one-dimensional spectrum (obtained by LST) where usually at most one unstable mode exists, multiple unstable modes are present in the global spectrum because of embodying the azimuthal dimension. Two distinguished branches of modes can be found: one consists of few modes and the other is composed of a sequence of modes. For the sake of convenience, we denote these two branches as branch D and branch S, respectively, and refer to modes of branch D as D modes and modes of branch S as S modes. Furthermore, the symmetric modes and antisymmetric modes in branch D are labeled as "mode V1, mode V2, …" and "mode A1, mode A2, …," respectively. Each symmetric mode appears to be paired with an antisymmetric mode. For branch D, mode V1 has the largest growth rate, followed by mode A1, mode V2, and mode A2. For branch S, the symmetric and antisymmetric modes are indistinguishable except for those with phase velocities larger than 0.825 where small discrepancies are noticeable. The closeness between the eigenvalues of symmetric and antisymmetric S modes originates in the fact that these modes lie a certain distance away from the symmetry plane (as will be shown later), and thereby are insensitive to the symmetry conditions. The shape functions of the three leading D modes are visualized in Figs. 6(b)–6(d). It can be inferred that all the modes lie in the vicinity of the
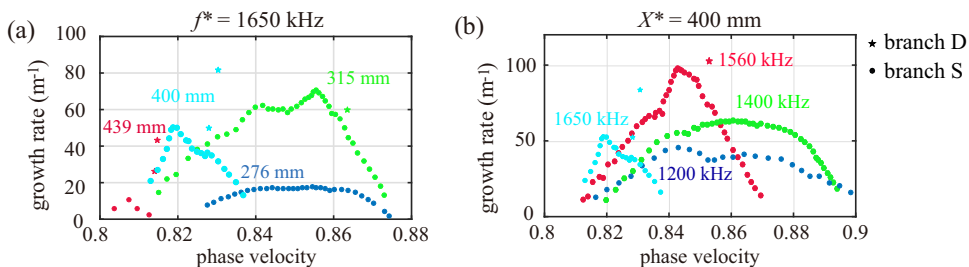
FIG. 7. Global eigenvalue spectra for (a) the frequency 1650 kHz at four axial stations ($X^* = 276$, 315, 400, and 439 mm) and (b) four frequencies ($f^* = 1200$, 1400, 1560, and 1650 kHz) at $X^* = 400$ mm.

windward ray; from mode V1 to mode V2, the disturbance progressively extends into the outboard region.

Since antisymmetric modes are less amplified and possess qualitatively the same stability characteristics as symmetric ones, we hereafter focus on the symmetric modes unless otherwise stated. The spatial structures of three representative S modes are visualized in Figs. 6(e)–6(g). Obviously, S modes lie in the outboard region, and particularly, the most amplified S mode lies closest to the windward ray than less amplified modes do. Moreover, all the S modes exhibit oblique wave fronts that are inclined at positive wave angles with respect to the ξ direction. Note that a positive wave angle corresponds to a positive azimuthal wave number n in LST. Hence, S modes in this half-plane [$\phi \in (0, 180)°$] appear to contain positive-n components only. However, LST results displayed in Fig. 5 indicate that positive-n and negative-n components are of equal importance for the Mack-mode instability. This discrepancy points out the essential difference between the local (LST) and global (BiGlobal) perspectives: while local modes at different azimuthal locations are independent in LST, global perturbations are coupled across the entire cone surface. Consequently, LST principally admits any azimuthal wave number, whereas only a particular subset of azimuthal wave numbers are allowed in BiGlobal. It is also worth noting that the azimuthal position of the mode S would move towards the windward ray with increasing frequency, due to the thinning of boundary layer approaching the windward ray. Figure 7 displays how the global eigenvalue spectra of the Mack-mode instability vary with the frequency and the axial station, respectively. One can observe that D modes are present only for large axial stations at a fixed frequency or high frequencies at a fixed axial station.

2. Relationship between D and S modes

In order to understand how the D and S modes are related, we examine the variation of D mode with temporal and spatial parameters. Following [49], we introduce a nondimensional frequency $F \equiv 2\pi f^*/(\mathrm{Re}^*_\infty U^*_\infty)$ (temporal parameter) and a local Reynolds number $R \equiv (\mathrm{Re}^*_\infty X^*)^{1/2}$ (spatial parameter). Figure 7 shows that branch D is present only for sufficiently large F at a fixed R or sufficiently large R at a fixed F. Therefore, we start at a large RF close to the neutral point of the D mode, and trace the D mode as RF decreases until it is indistinguishable from the S modes. Figures 8(a) and 8(b) show the distributions of the growth rates and phase velocities of mode V1 of branch D, which include the following two computational cases:

Case 1: growth rates and phase velocities as a function of different frequencies F at a fixed streamwise location of $R = 2884$ ($X^* = 400$ mm).

Case 2: growth rates and phase velocities as a function of different streamwise locations R at a fixed frequency of $F = 2.8 \times 10^{-4}$ ($f^* = 1650$ kHz).

The figure shows that the two cases have qualitatively similar curves when they are plotted as functions of RF. The similarity between such two cases has also been observed by Ma and
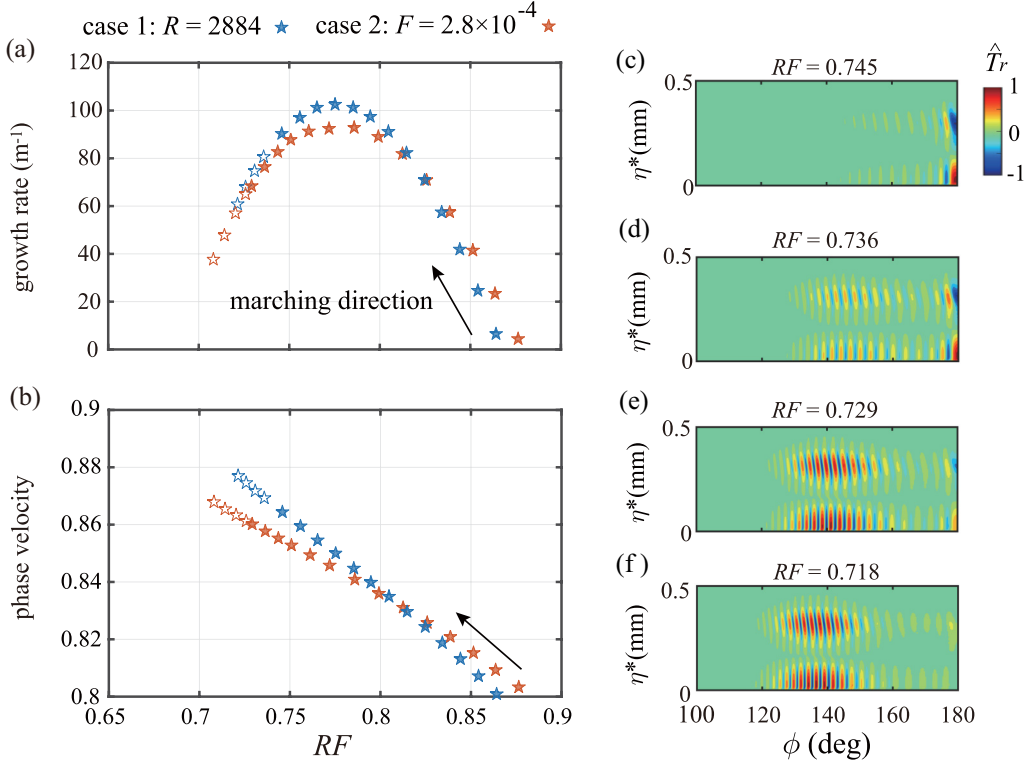
FIG. 8. The distribution of the growth rates (a) and phase velocities (b) of the D mode (mode V1, filled symbols) as a function of RF, either at different frequencies with a fixed location (case 1, $R = 2884$, $X^* = 400$ mm) or at different streamwise locations with a fixed frequency (case 2, $F = 2.8 \times 10^{-4}$, $f^* = 1650$ kHz). The results are obtained by BiGlobal marching from right to left. Hollow symbols are mixed modes of branch S which are the continuation of mode V1. (c)–(f) Temperature eigenfunctions of four successive frequencies of case 1.

Zhong [49] in studying stability of a supersonic flat-plate boundary layer, and probably arises from the self-similarity of the boundary layer.

Take case 1 for example. As RF decreases, mode V1 turns into a mixed S mode at $RF \approx 0.736$. Mixed S mode here means that the mode almost merges with branch S yet has noticeable fluctuations in the vicinity of the windward ray. At $RF \approx 0.72$, the normalized mode amplitude at the windward ray has dropped below 0.2, and the mode can thus be viewed as a pure S mode. This conversion process is clearly characterized by the variation of eigenfunctions with RF in Figs. 8(c)–8(f). Mode in case 2 undergoes a similar process but with a smaller transition threshold of RF. Therefore, we conclude that branch D originates in branch S.

Before proceeding further, it is of interest to compare the present results with researches on similar configurations. Considering a sharp yawed cone under a wind-tunnel condition, Paredes *et al.* [9] identified one planar Mack mode peaking at the windward ray and few oblique Mack modes in the outboard region. The eigenfunction features suggest that these two types of Mack-mode instabilities are analogous to branch D and branch S in this study, respectively. Nevertheless, the peak growth rates and frequencies in Paredes's case are much smaller, likely due to the difference between the wall-temperature ratios of two studies. On the other hand, since the boundary-layer flow in the vicinity of the windward ray is somewhat like the classical attachment-line flow, the stability characteristics for these two flow configurations also bear some similarities. For example,

TABLE II. BiGlobal modes serving as initial conditions of PSE3D.

Case	C1 C2 C3 C4 C5 C6	C7	C8
Inlet locations	$X^* = 300$ mm	$X^* = 303$ mm	$X^* = 322$ mm
Mode type	Pure S mode	Mixed S mode	D mode

alternatively arranged symmetric and antisymmetric modes emerge in branch D, resembling the hierarchy of the attachment-line modes [50–52]; and the predominance of the Mack-mode instability has also been observed in the proximity of the attachment line [20,53]. Furthermore, because the boundary-layer flow in the outboard region is featured by the crossflow, the branch S modes therein closely resemble the oblique Mack modes identified in crossflow regions of the elliptic cone [53] and of the lifting body [20]. The comparison above points out another distinction between the D and S modes, that is, the former is in essence an attachment-line instability, whereas the latter is a crossflow-dominated instability.

3. Linear spatial evolution of global mode

Below we utilize PSE3D to investigate the spatial development of Mack-mode waves, initiated by various BiGlobal modes at frequency 1650 kHz as listed in Table II. Due to multiplicity of modes, many routes are possible for a single frequency. In this paper, we consider three types of initial modes, that is, pure S modes at $X^* = 300$ mm (C1–C6) labeled in Fig. 9(a) as C1 through C6 with an increasing initial phase velocity, the most upstream mixed S mode (C7) and the most upstream D mode (C8). The corresponding PSE3D results are displayed in Figs. 9(b)–9(d). The PSE3D calculation terminates when the growth rate becomes negative. In all the cases, the phase velocities decrease all the way to the outlet. The amplification rates for the first three cases, C1–C3, also monotonically decay, resulting in a small integrated growth rate $N \equiv \int -\alpha_i d\xi < 2$. In case C4, the disturbance is mildly enhanced, followed by a slightly destabilizing stage. Disturbances in cases C5 and C6, on the other hand, both experience a notably promotion beyond $X^* \approx 370$ mm. The growth rates and phase velocities in cases C5 and C6 gradually approach the branch D modes (modes V1 and V2) for $X^* > 420$ mm, implying that the S modes in these cases eventually develop into D modes. Such a conversion process can be readily seen by the evolution of spatial structures as shown in Figs. 10(b) and 10(c). For case C5, a noticeable shift of the spatial distribution from the outboard region to the region close to the windward centerline is observed. Near the outlet, two distinct regions exist; one peaks at the windward ray and the other lies a small distance away, exhibiting a flow pattern formed by a mixture of modes V1 and V2. Case C6 undergoes a similar modal structure transition as case C5 and, furthermore, the disturbance magnitude in the outboard region gradually decreases to a negligibly small level relative to the center-line peak so that the fluctuations are eventually dominated by mode V1. In comparison, disturbances in case C2 remain in the outboard region, slightly moving towards the windward ray downstream due to the thickening of the boundary layer. The largest N factor, slightly beyond 5, is reached by case C6. Tests (not shown here) indicate that forcing disturbances at a more upstream station leads to qualitatively similar results but with smaller peak N factors. By contrast, case C7 starts immediately downstream of cases C1–C6, and yet the modal growth rate increases rapidly and reaches the same level as mode V1 much earlier than in cases C5 and C6, thereby achieving a substantially larger N factor. This is because the inlet mode in case C7 possesses significant fluctuations in the vicinity of the windward ray that could efficiently excite mode V1. Although disturbance in case C8 immediately follows the route of mode V1, the amplification region is shorter so that the maximum N factor of case C8 is slightly smaller than that of case C7.

The above results indicate that initially seeding the most upstream mixed mode yields the largest N factor. Forcing a pure S mode in a more upstream station or a D mode in a more downstream station as an inlet mode leads to smaller N factors because of a longer transformation distance or
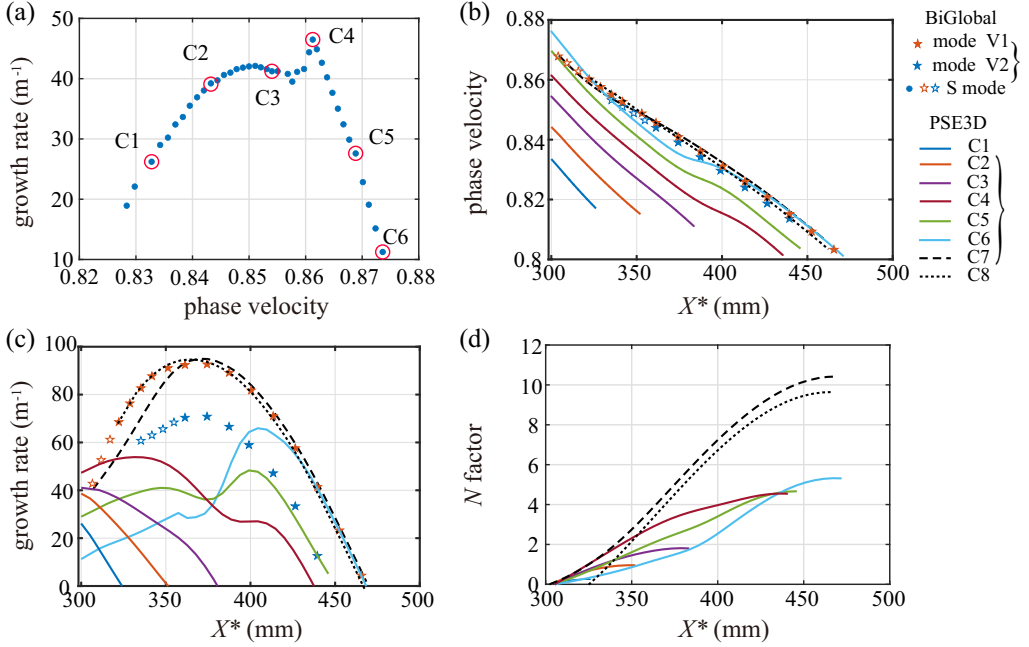
FIG. 9. (a) Global eigenvalue spectrum for frequency 1650 kHz at $X^* = 300$ mm with six modes (as marked by circles) separately serving as the inlet mode of PSE3D calculation cases C1–C6. Spatial evolution of the corresponding cases are displayed in terms of (b) phase velocity, (c) growth rate, (d) N factor ($N \equiv \int -\alpha_i d\xi$) as function of axial stations. The results of case C7 initiated by the most upstream mixed mode and of case C8 initiated by the most upstream branch D mode are also shown for comparison, along with the traces of modes V1 and V2 of branch D (filled symbols) and the mixed modes of branch S (hollow symbols) obtained by BiGlobal.

a shorter integration path. The above results also qualitatively hold for other frequencies as well as the antisymmetric modes. Therefore, by imposing the most upstream mixed mode in the inlet of PSE3D, we obtain the most amplified N factors for various frequencies, as shown in Fig. 11. With increasing frequency, the N-factor curve moves rearward, in accord with the growth of the boundary-layer thickness, and reaches higher peak values. For comparison, we also display the N-factor result of the antisymmetric mode of frequency 1650 kHz. Obviously, the antisymmetric mode is less amplified than the symmetric counterpart.

The above results of spatial developments of global Mack-mode instabilities lead to an important conclusion that the Mack mode itself is not dangerous in the outboard region, but can potentially trigger the boundary-layer transition in the vicinity of the windward plane. This conclusion is also partially supported by the DNS results by Yang [27] (see Appendix C). Therefore, the transition front is expected to be indented and be restricted to the small region close to the windward ray as observed in flight tests as well as some ground tests.

C. Nonlinear development of the Mack mode and resonance mechanisms

As shown above, the D modes are most amplified that might induce the boundary-layer transition. In the following, we continue to explore weakly nonlinear mechanisms in the stage when a symmetric or an antisymmetric D mode becomes large enough in amplitude. To begin, we inspect the shape function that (except for the azimuthal velocity) can be represented by a series of cosine
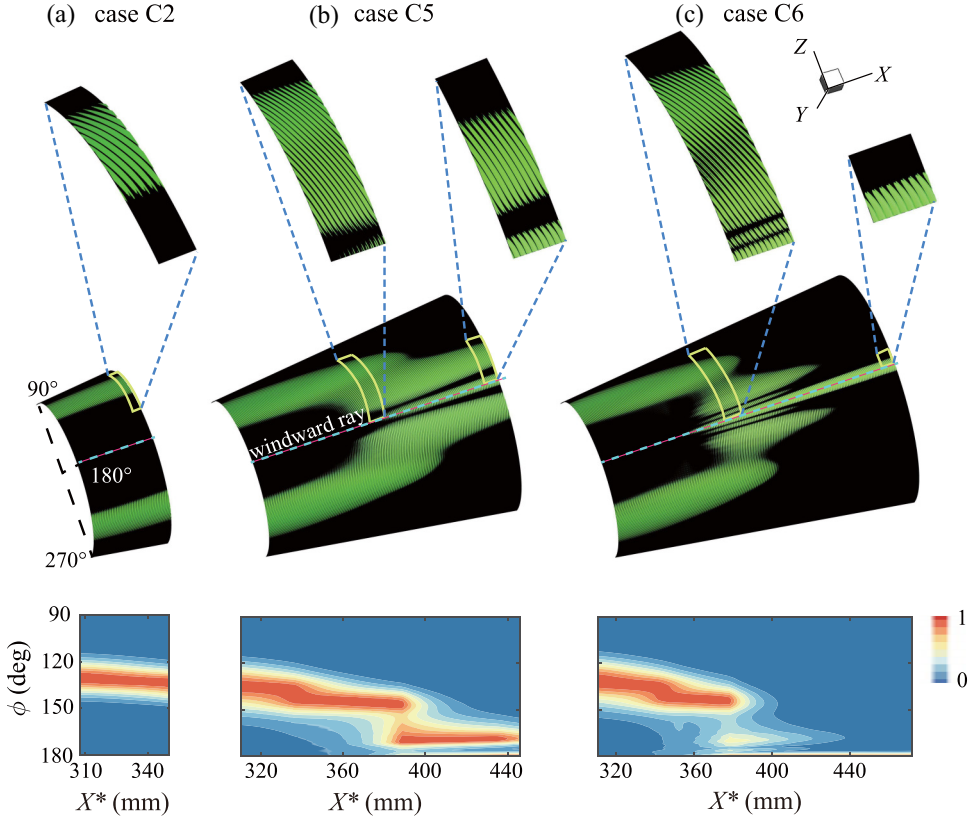
FIG. 10. Three typical types of spatial developments of Mack-mode waves illustrated by cases C2, C5, and C6. (a) Case C2: perturbations are dominated by modes of branch S. (b) Case C5: perturbations are eventually dominated by a mixture of modes V1 and V2 of branch D. (c) Case C6: perturbations are eventually dominated by mode V1 of branch D. The spatial structures are visualized by isosurfaces of the real part of the normalized temperature perturbation $\hat{T}_r$ at the contour level of 0.2. Half of the cone surface ($\phi \in [90, 270]°$) is shown. The windward center line is denoted by the dashed line. The zoomed-in views display details of the spatial structures near the outlet and in the transitional regions. The bottom row of plots show the distribution of the reduced temperature perturbation $\max_\eta[\hat{T}(\xi, \eta, \phi)|]/\max_\phi (\max_\eta[|\hat{T}(\xi, \eta, \phi)|])$ in the X^*-ϕ plane.
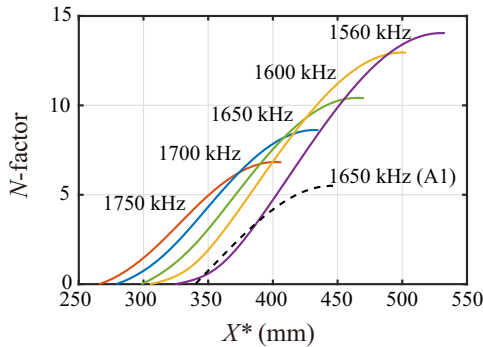
FIG. 11. Development of N factors of Mack-mode waves of various frequencies (labeled in plot) from PSE3D initiated by the most upstream mixed mode of each frequency. The N-factor curve for the antisymmetric case of frequency 1650 kHz is also displayed for comparison.
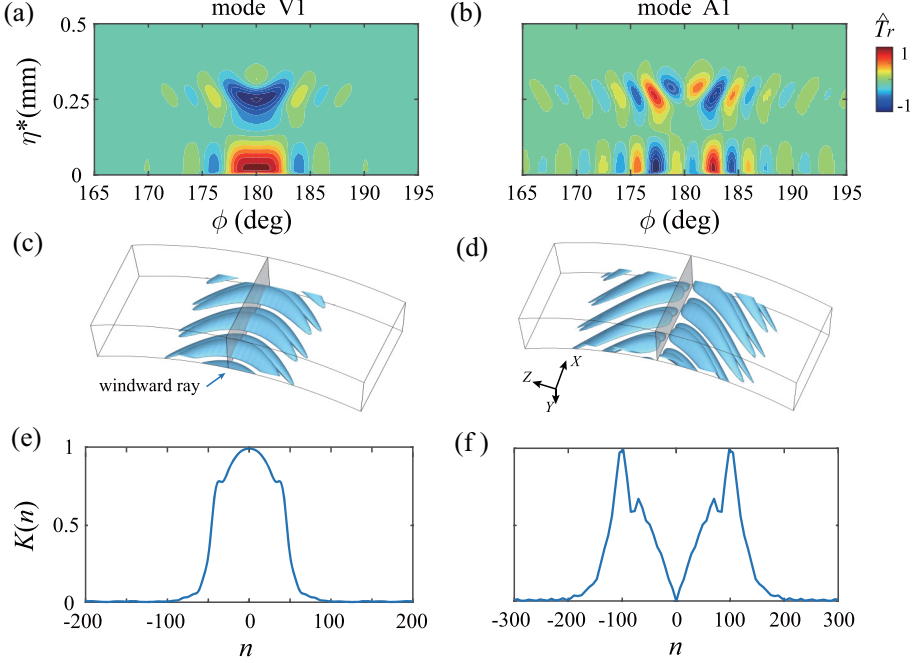
FIG. 12. Features of the (temperature) shape functions of leading symmetric D mode (V1) at $X^* = 322$ mm (a), (c), (e) and of the leading antisymmetric D mode (A1) at $X^* = 354$ mm (b), (d), (f). (a), (b) The real part. (c), (d) The spatial structures illustrated by isosurfaces of $\text{Re}[\hat{T}(\eta, \zeta) \exp(i\alpha\xi)]$, with value of 0.2. (e), (f) The azimuthal wave-number spectrum. The mode frequency is set to 1650 kHz.

functions of the azimuthal angle,

$$\hat{q}_s(\eta, \zeta) = \hat{q}_0(\eta) + \sum_{n \neq 0} \hat{q}_n(\eta) \cos(n\phi), \quad \phi \in [0, 2\pi], \tag{19}$$

for the symmetric mode, and by a series of sine functions of the azimuthal angle,

$$\hat{q}_a(\eta, \zeta) = \sum_{n \neq 0} \hat{q}_n(\eta) \sin(n\phi), \quad \phi \in [0, 2\pi], \tag{20}$$

for the antisymmetric mode. $\hat{q}_0(\eta)$ in (19) is equivalent to the planar Mack mode in the context of the one-dimensional stability analysis. Further define the azimuthal wave-number spectrum of the shape function $K(n)$ as

$$K(n) \equiv \max_{\eta} |\hat{q}_n(\eta)| / \max_{n}[\max_{\eta} |\hat{q}_n(\eta)|] \in [0, 1], \tag{21}$$

to describe the relative importance of the cosine and sine components.

Figure 12 shows the real parts of the temperature shape functions, the reconstructed spatial structures, and the corresponding azimuthal wave-number spectra for the leading symmetric D mode (V1) of 1650 kHz and the leading antisymmetric D mode (A1) with the same frequency at the axial locations where these modes just separate from branch S. Obviously, the symmetric mode is dominated by the planar component associated with $n = 0$, whereas the antisymmetric mode is dominated by the oblique components at $n \approx \pm 100$. Also observe that modal structures gradually bend backward as they extend into the outboard region, with opposite local wave angles on two sides of the windward ray.
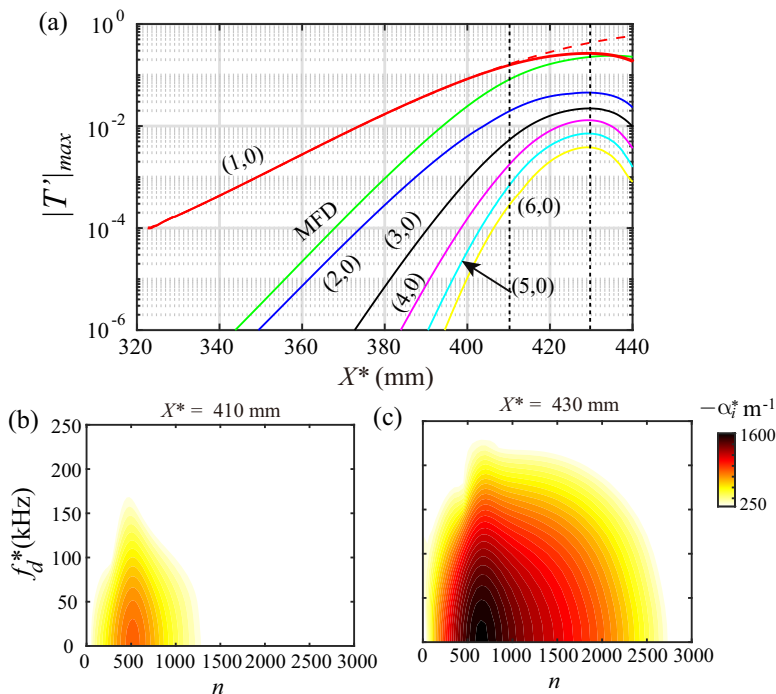
FIG. 13. (a) Streamwise development of the maximum temperature disturbance amplitude from NPSE2D results. The planar Mack-mode wave at frequency 1650 kHz is forced with an initial amplitude of 0.01%. The dashed line denotes the linear case. Growth rates of the secondary-instability modes predicted by Floquet theory as functions of the difference-mode frequency (f_d^*) and the azimuthal wave number (n) at (b) $X^* = 410$ mm and (c) $X^* = 430$ mm [marked by the dotted lines in (a)]. Only growth rates larger than 250 m^{-1} are displayed to highlight the most unstable region.

Self-interactions of global modes yield harmonics and a stationary mode. The symmetry features of these nonlinearly generated modes are obvious: those in the symmetric-mode case are symmetric too; those in the antisymmetric-mode case divide into two groups, that is, the nonlinearly generated modes with frequency of $2mF$ ($m = 0, 1, 2, \dots$) are symmetric and those with frequency of $(2m + 1)F$ are antisymmetric. Below we will separately examine the nonlinear developments of the leading symmetric and antisymmetric modes, which are hereafter denoted as the symmetric-mode case and the antisymmetric-mode case, respectively.

1. Nonlinear development of the leading symmetric D mode

The predominance of the planar component suggests that the nonlinear development of mode V1 can be represented, as a zeroth-order approximation, by the nonlinear evolution of a local planar Mack mode at the same frequency. Figure 13(a) shows the amplitude development of the planar Mack mode (primary mode) at frequency 1650 kHz, the mean flow distortion (MFD), and several harmonics in the presence of self-interactions, obtained by NPSE2D marching along the windward ray. Five harmonics are included in the calculation, and are sufficient to obtain converged results. Unless otherwise stated, the primary mode is forced at $X^* = 322$ mm with an initial amplitude (based on the temperature fluctuation) of 0.01%. The initial amplitude of the corresponding pressure fluctuations (normalized by the static pressure) is below 0.05%, which is far below the pressure fluctuation level (0.1%) in typical quiet wind tunnels [54]. It can be clearly seen that the primary

mode departs from the linear case at $X^* \approx 400$ mm, becoming saturated and eventually slowly decaying for $X^* > 430$ mm.

Subsequent Floquet analysis for the saturated flow field indicates that combination resonances with nonzero difference frequencies ($0 < f_d^* < 200$ kHz) and fundamental resonances (for $f_d^* = 0$) are active, and the latter are always stronger than the former. The amplification rates of secondary instabilities at two presentative axial stations are visualized in Figs. 13(b) and 13(c). The secondary instabilities at the second station appear much stronger than those at the upstream station, presumably owing to changes of the primary mode amplitude and the mode shape. Predominance of the fundamental resonance is consistent with previous studies [13,36,55,56] on axisymmetric configurations, and yet remarkable differences exist. While the maximum secondary-instability amplification rates documented in previous studies are generally below 200 m^{-1} with the corresponding azimuthal wave number generally smaller than 100, in the present case the growth rates of secondary-instability modes can be as large as 1600 m^{-1}, approximately 16 times larger than those of the primary wave, with the peak azimuthal wave number around 600. As such, an abrupt breakdown of the Mack-mode waves is expected once the secondary instability sets in. From the global point of view, the global Mack mode inherently contains both planar and oblique components, hence is expected to trigger secondary instabilities without additionally seeding three-dimensional (3D) disturbances. To confirm this speculation, we further investigate the nonlinear evolution of the global Mack mode via NPSE3D. Mode V1 of branch D with frequency of 1650 kHz serves as the inlet condition of NPSE3D. The inlet location and initial amplitude are prescribed to be the same as in the NPSE2D case (Fig. 13). The primary mode (denoted by $1F$) simultaneously generates a stationary mode ($0F$) and harmonics ($mF, m > 1$) through self-interactions. Only one harmonic is considered in the calculation, which already leads to converged results as shown in Appendix B. The computation domain covers an azimuthal region from $\phi = 168°$ to $180°$ and is resolved by 101 wall-normal points and 200 azimuthal points (of which 120 points are distributed in the range from $\phi = 178°$ to $180°$). The domain size and grid resolution have been tested to ensure the convergence of results (see Appendix B). Symmetric boundary conditions are utilized at the windward ray, while Dirichlet boundary conditions are assumed at the outboard azimuthal boundary since the fluctuation amplitudes are negligibly small there.

Figure 14(a) displays the downstream development of the primary mode and several nonlinearly generated modes. It can be seen that these modes amplify at nearly constant growth rates until $X^* \approx 400$ mm where the stationary and primary mode amplitudes start to grow at higher growth rates. At $X^* \approx 402$ mm, the stationary mode amplitude surpasses the primary mode amplitude, and the harmonic also begins to amplify much faster than before. The stationary and primary modes get saturated at $X^* \approx 405$ mm. Comparison with the NPSE2D results considering only self-interactions indicates that the early stage of the nonlinear development of the global Mack mode is mainly characterized by self-interactions of its planar component, while the late stage is featured by a totally different instability mechanism.

The downstream development of the time-averaged skin friction coefficient along the windward ray is shown in Fig. 14(b). The skin friction coefficient was calculated as

$$C_f = \frac{2(\bar{\mu}\partial\bar{U}_t/\partial\eta)_w}{\mathrm{Re}}, \tag{22}$$

where $\bar{U}_t$ denotes the streamwise velocity of the temporally averaged base flow. The skin friction coefficient curve obtained from NPSE3D is compared with a turbulent boundary-layer correlation from White [57]. It can be seen that the skin friction coefficient initially follows the laminar curve up to $X^* \approx 400$ mm, then rises steeply afterwards, and finally drops as the stationary mode saturates. In comparison, the skin friction curve of NPSE2D results increases rather mildly. In order to understand the instability mechanism of the rapid growth of the stationary mode in the late stage, we further assess the amplitude evolutions of the azimuthal components of the primary and stationary modes, as shown in Fig. 15. The most prominent feature is that some high-order azimuthal components ($n > 200$) of both modes begin to amplify obviously faster beyond $X^* \approx 390$ mm, a
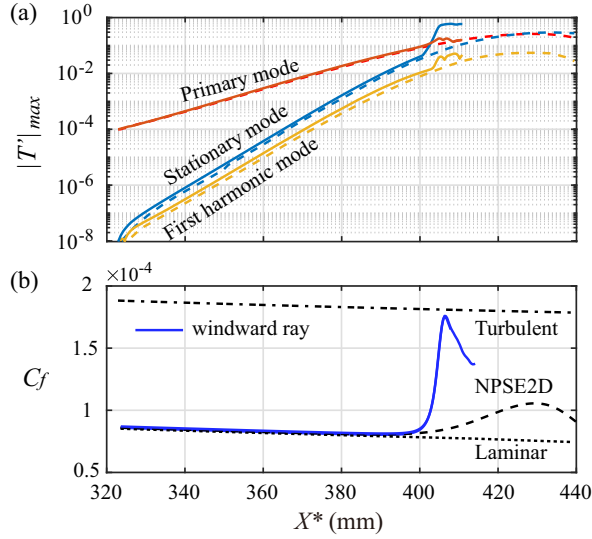
FIG. 14. (a) Nonlinear development of the maximum temperature disturbance amplitude obtained from NPSE3D. The global D mode at frequency 1650 kHz is forced with an initial amplitude of 0.01%. Results of the stationary mode and first harmonic are displayed. The NPSE2D results in Fig. 13 (dashed lines) are also shown for comparison. (b) Development of the time-averaged skin friction coefficient along the windward ray, together with the laminar curve (dotted line), turbulent curve (dashed-dotted line), and the NPSE2D case with self-interactions only (dashed line).

signature of secondary instability. More specifically, the growth rates of components in the range of $200 < n < 800$ are close to those of fundamental-resonance instabilities predicted by the Floquet theory. These high-order azimuthal components progressively interact with low-order azimuthal components, causing the rapid growth of global modes. Note that until the very late stage of the
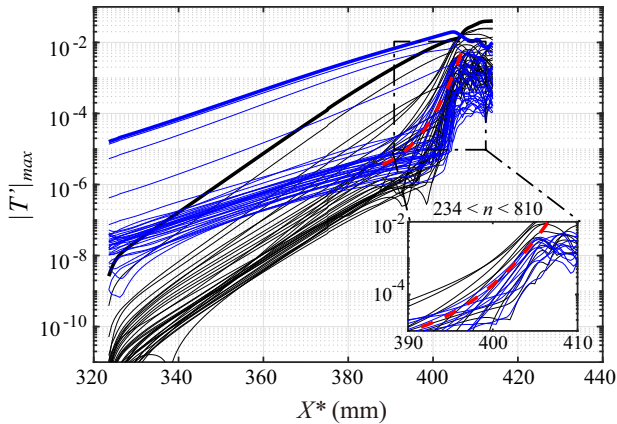

FIG. 15. Streamwise development of the maximum temperature disturbance amplitude for each of the azimuthal components in a range of $n \in (0, 1800)$ with an increment of 54 for the primary mode (blue lines) and the stationary mode (black lines). The planar component and the MFD are thickened. A zoomed-in plot displays the late-stage amplitude evolution of the azimuthal components with $234 < n < 810$, highlighting the secondary-instability stage. The fundamental secondary-instability amplifications for $n = 500$ predicted by the Floquet analysis are also included (red dashed line) for comparison.
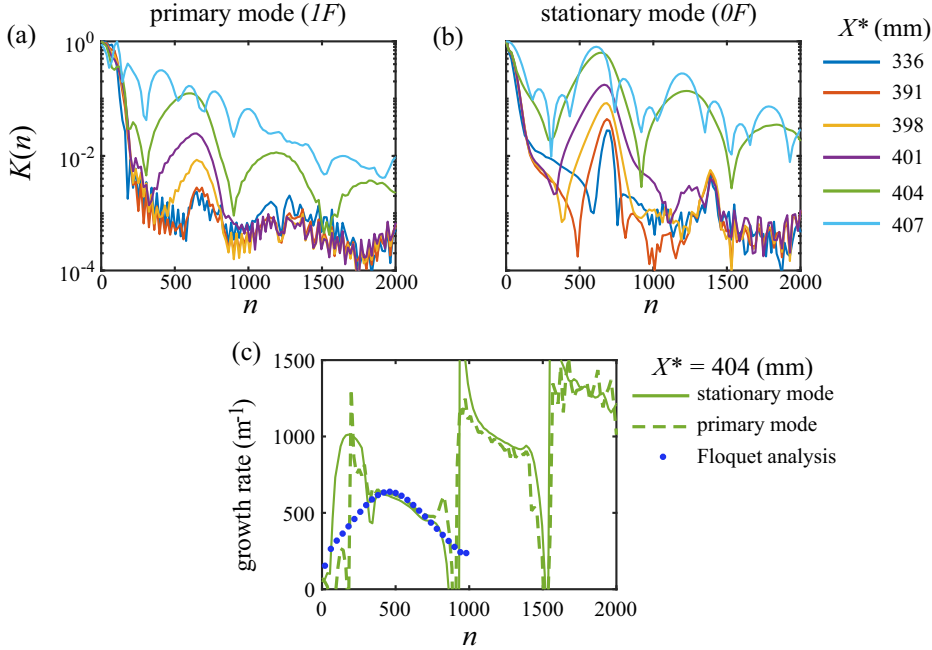
FIG. 16. Downstream evolution of the azimuthal wave-number spectra of the primary mode (a) and the stationary mode (b) for six representative axial stations. The growth rate distributions at the fifth station ($X^* = 404$ mm) are shown in (c), together with the growth rate distribution predicted by the Floquet analysis (symbols) for comparison.

calculation the growth rates of all the azimuthal components of the primary mode are still positive, even though the oblique components with moderate and large azimuthal wave numbers ($n > 200$) are stable according to LST (see Fig. 5). This is likely because of the azimuthal inhomogeneity of the base flow which is neglected by LST but is fully considered by the global counterparts (BiGlobal and PSE3D). As such, oblique components are coupled with the planar component, and propagate downstream as a whole. In an attempt to provide a more convincing evidence on the secondary instability, we display the azimuthal wave-number spectra defined in Eq. (21) for the primary and stationary modes at several axial stations in Figures 16(a) and 16(b). It can be seen that the spectrum of the primary mode is initially governed by the low-order components ($n < 200$) in addition to a small secondary peak at $n \approx 700$. The normalized spectrum remains nearly unchanged until $X^* = 398$ mm where the secondary peak starts to amplify, expands rapidly, and shifts slightly towards lower azimuthal wave numbers. At $X^* = 404$ mm, high-order harmonic peaks become visible, and fill up rapidly in wave-number space. Likewise, the stationary mode initially exhibits a primary peak at $n = 0$, which corresponds to the MFD, and a secondary peak at $n \approx 700$, which reflects the initial preference of the azimuthal wave number due to the self-interaction of the primary mode. Beyond the second axial station, the secondary peak also strengthes rapidly, leading to a fast spectral broadening.

The growth rate distributions of the primary and stationary modes with respect to the azimuthal wave number are shown in Fig. 16(c) for $X^* = 404$ mm. One can observe that the growth rates of these two modes nearly coincide for $n > 300$, where three distinct plateaus form. The first plateau lies in the range of $n \in (300, 800)$, while the other two plateaus, in the ranges of $n \in (1000, 1400)$ and $n \in (1500, 2000)$, are apparently the harmonics of the former one. Recall that in the secondary-instability stage, the secondary modes will amplify at identical rates [see Eq. (16)]. The closeness between growth rates of the primary and stationary modes in the range of $n > 300$ is a strong
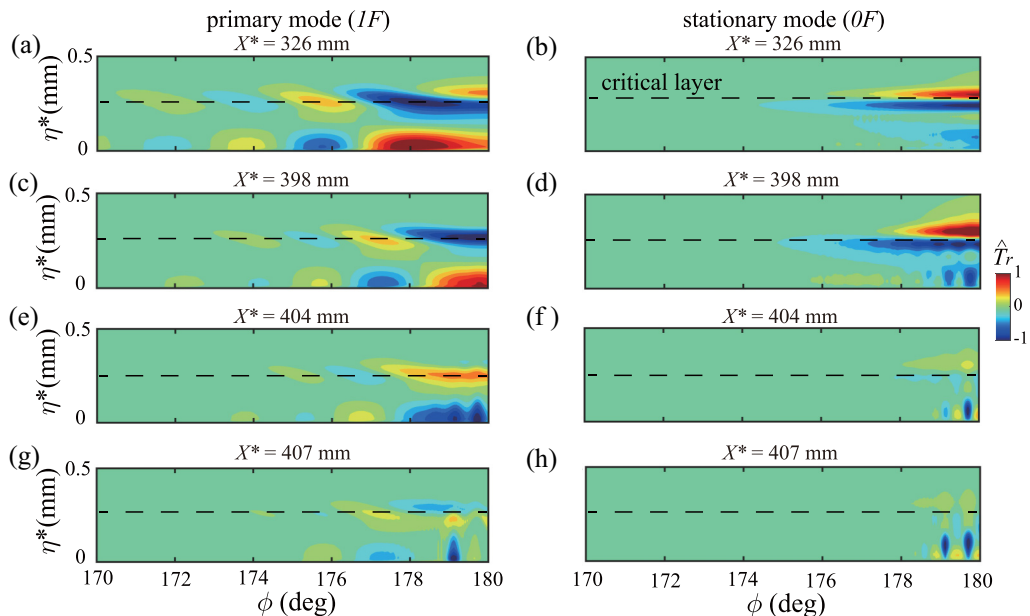
FIG. 17. Real parts of the normalized temperature shape functions of the primary mode [the left column, (a), (c), (e), (g)] and the stationary mode [the right column, (b), (d), (f), (h)] at four representative axial locations. The critical layer of the Mack mode [y_c, where $U(y_c) = c$, c the phase velocity of Mack mode] is also displayed (dashed line).

evidence of the presence of the fundamental resonance. Moreover, the growth rates of the first plateau match reasonably well with those from the Floquet analysis, confirming the ability of the Floquet theory in adequately capturing the fundamental secondary instability of the symmetric D mode. Figure 17 shows the real parts of the normalized temperature shape functions of the primary and stationary modes at four representative axial locations. Initially, the stationary mode concentrates in the critical layer where nonlinear effects are most prominent [58]. At the next station, alternating high- and low-thermal regions manifest themselves in the near-wall region, and rapidly take over the fluctuation distribution, forming high- and low-thermal streaks. The streak amplitude decreases fast away from the windward ray, and the streak spacing is approximately 0.6° corresponding to an azimuthal wave number of around 600. The Mack mode begins to feel the feedback effects of the stationary mode from the third station and, as a result, its modal structure breaks down in the vicinity of the windward ray at the last station. The late-stage development of three-dimensional flow structures reconstructed by the primary and stationary modes is shown in Fig. 18. It can be seen that slightly bending spanwise rolls emerge and exhibit a significant spreading in the azimuthal direction as the primary mode amplitude amplifies. Farther downstream, noticeable azimuthal modulation appears in the vortical structures, inducing strong streamwise vorticity with alternating signs and streaky structures in the velocity isosurface. Particularly along the windward ray, a high-speed streak and a high-thermal streak (corresponding to a peak Stanton number) develop. This flow pattern is reminiscent of what is observed for the 3D wave packet on a flared cone at zero angle of attack [14].

According to the study by Hader and Fasel [59], the fundamental breakdown scenario in an axisymmetric configuration is characterized by the initial appearance of "primary" streaks and the subsequent emergence of "secondary" streaks prior to final breakdown to turbulence. Accordingly, the skin friction coefficient first undergoes a significant rise caused by the primary streaks, then drops off (because of attenuation of the primary streaks) and eventually steeply lifts up when
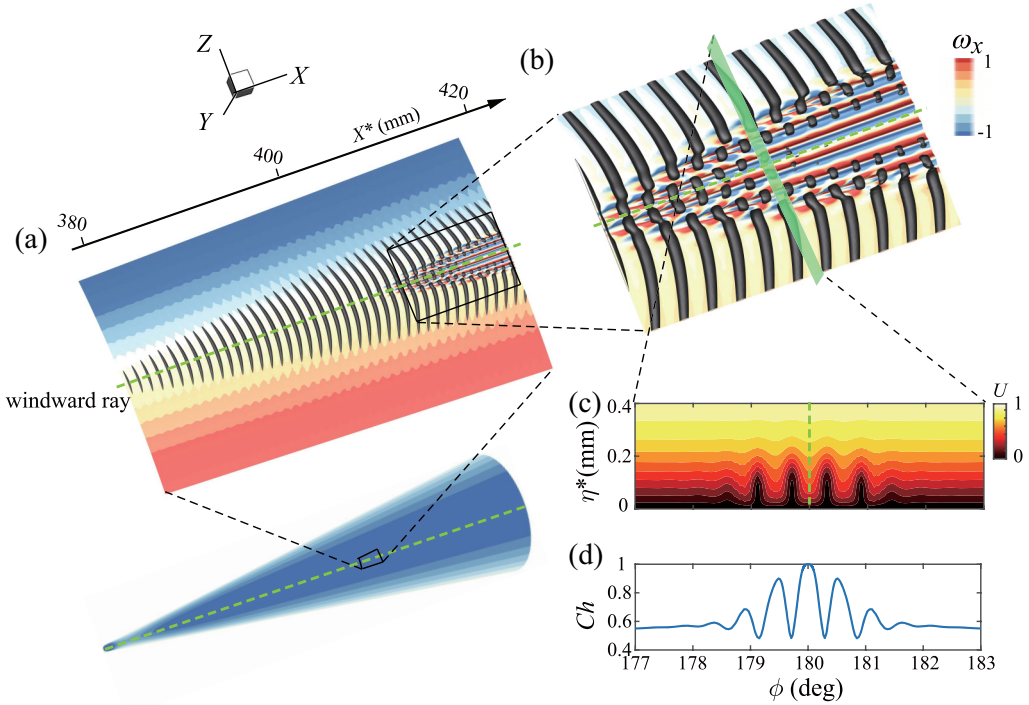
FIG. 18. Late-stage instantaneous flow pattern from NPSE3D calculations for the symmetric-mode case. (a) Vortical structures visualized by the isosurface of Q criterion ($Q = 0.1$), along with isosurface of the axial velocity ($U = 0.2$) colored by the normalized axis vorticity (ω_x). (b) Zoomed-in image of the spatial structure corresponding to the squared region in (a). (c) The normalized axial velocity in the cross section at the middle of the region ($X^* = 407$ mm) in (b). (d) Normalized time-averaged Stanton number distribution in the azimuthal direction.

the secondary streaks begin to appear. In analogy to their results, the theoretical calculations in this study capture the primary-streak stage but miss the secondary-streak stage. Note that the secondary-streak stage is featured by the rapid growth of broadband disturbances arising from numerical or ambient noises in simulations or experiments. Whereas the fundamental resonance only provides a spectral-broadening mechanism essentially in the azimuthal wave-number space, two other mechanisms, namely, the combination resonance and the streak instability, are likely important ingredients in filling up the spectrum in the frequency space.

The combination resonance likely occurs in the side-band interactions of the Mack-mode waves. In this study, we separately force at the inlet of NPSE3D a side-band mode at various frequencies (denoted by f_s^*) with an initial amplitude of 10^{-5}, in addition to the primary mode with the same conditions as the self-interaction case studied above. The primary mode and the side-band mode simultaneously generate a difference mode at frequency ($f_d^* = f_p^* - f_s^*$) and a sum mode at frequency ($f_p^* + f_s^*$). Figures 19(a) and 19(c) show the amplitude evolutions of representative modes in two side-band-interaction cases. One can observe that the fundamental resonance between the primary mode and the stationary mode is always present, and is seemingly unaffected by the side-band interactions. The sum mode starts with a much smaller amplitude but a notably larger growth rate than the difference mode. Once the sum mode amplitude becomes comparable to the difference mode amplitude, the difference mode begins to amplify remarkably faster than before, exhibiting a turning point in the amplitude curve, and eventually promotes the side-band mode. This rapid growth stage of the combination modes stops where the primary and stationary modes saturate.
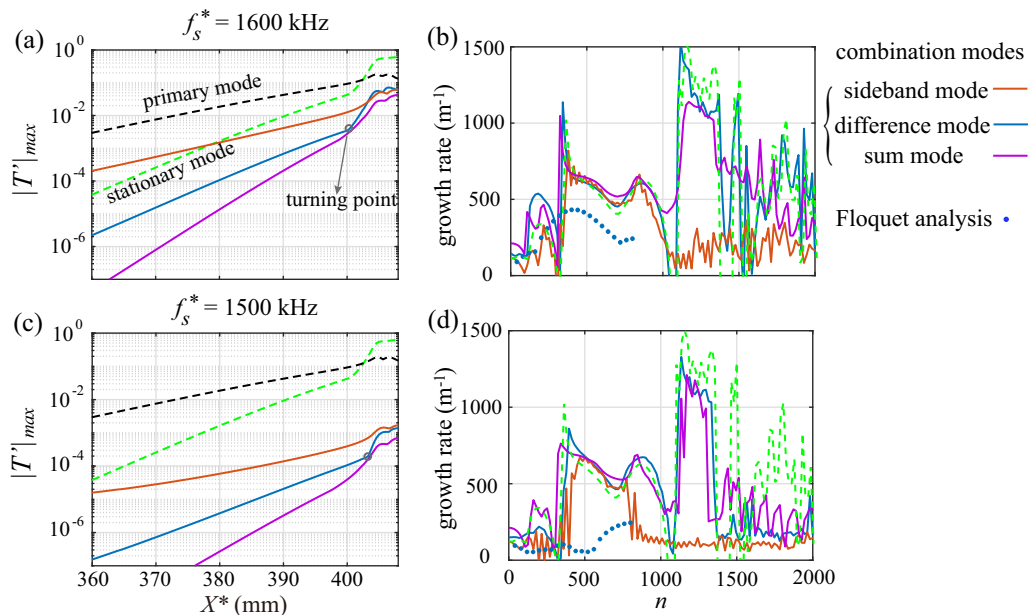
FIG. 19. Results of interactions between the primary mode (1650 kHz) and a side-band mode with different frequencies: (a), (b) 1600 kHz, (c), (d) 1500 kHz. The modal amplitude evolutions are shown in the left column, while growth rate distributions at $X^* = 401$ mm for the combination modes are displayed in the right column along with the growth rate distribution for the stationary mode (dashed line) and the Floquet analysis results (dots) for comparison.

As the frequency difference between the primary mode and the side-band mode is increased, the turning point of the amplitude curve of the difference mode moves rearward, and the saturated amplitude level of the combination modes is significantly decreased.

The growth rate distributions over the azimuthal components for the combination modes at $X^* = 401$ mm are displayed in the right column of Fig. 19. It can be seen that the growth rates are almost coincident in the range of $n \in (300, 800)$, indicating that these oblique components are actually in resonance. Interestingly, the growth rates in this azimuthal wave-number range are as large as those of the fundamental modes, and are insensitive to the frequency difference, contradicting what the Floquet theory predicts. This observation suggests that the resonant growth of the combination modes is not only ascribed to the planar component of the primary mode as in the Floquet theory, but is also driven by the fundamental-resonance oblique components.

At last, we point out that the fundamental resonance is robust to the initial amplitude and the mode frequency: it occurs once the primary mode temperature amplitude exceeds 10% of the free-stream value, as shown in Appendix D.

2. Nonlinear development of the leading antisymmetric D mode

Although the antisymmetric D mode is much less amplified than the symmetric counterpart, it can still play an important role in noisy environments. The absence of the planar component suggests that the fundamental resonance is no longer relevant in the nonlinear development of this mode. Moreover, the modal structure in either side consists mainly of oblique components with the same sign, as evidenced in Fig. 12, so that oblique breakdown comprising of a pair of oblique waves with equal but opposite wave angles is deemed inactive too. Therefore, whether this mode will lead to the laminar flow breakdown needs to be explored further. Contrary to the symmetric counterpart, the antisymmetric mode shape covers a wider azimuthal domain yet is less concentrated as indicated
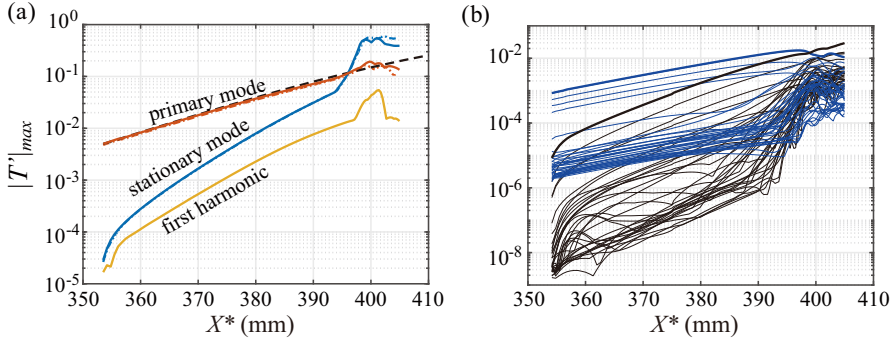
FIG. 20. (a) Nonlinear development of the maximum temperature disturbance amplitude of the leading antisymmetric D mode at frequency 1650 kHz, together with results of the stationary mode and the first harmonic. NPSE3D results adopting Dirichlet conditions for all variables at the windward ray are also shown for the primary and stationary modes (dashed-dotted lines). Dashed line represents linear PSE3D results. (b) Development of the maximum temperature disturbance amplitude for each of the azimuthal components in a range of $n \in (0,1200)$ with an increment of 36 for the primary mode (blue lines) and the stationary mode (black lines). The thick lines stand for the dominant components of the primary mode ($n = 108$) and stationary mode (MFD).

in Fig. 12(b), rendering the line-marching approach (NPSE2D) along a particular ray inappropriate. Thus, we directly utilize NPSE3D to study the nonlinear development of the antisymmetric mode.

In this case, the inlet location is set to be at $X^* = 353$ mm close to the most upstream location of the antisymmetric D mode at this frequency, and a larger initial amplitude (0.5%) is used to accelerate the nonlinear process. The NPSE3D are solved with 200 azimuthal points nonuniformly distributed within an azimuthal domain of $\phi \in (162, 180)°$ and 101 wall-normal points. The downstream developments of significantly amplified modes are displayed in Fig. 20(a). One can see that once the primary mode amplitude exceeds 10%, just the same threshold of fundamental resonance, the stationary mode starts to amplify substantially faster than before, and soon becomes a dominant mode followed by a saturated state.

Amplitude evolutions for azimuthal components of the primary and stationary modes are visualized in Fig. 20(b). Exponential growth is observed for all the azimuthal components of the primary mode in the early stage. In contrast, the azimuthal components of the stationary mode initially experience a transient growth stage; subsequently, some azimuthal components enter into an exponential stage with growth rates almost twice of the primary counterparts, while others follow an irregular development path; beyond $X^* > 380$ mm, some high-order azimuthal components of the stationary mode begin to amplify faster, further promoting high-order azimuthal components of the primary mode. For $X^* > 400$ mm, all the components get saturated and are fully coupled. To demonstrate how the energy is distributed in the azimuthal wave number at different downstream locations, the amplitude spectra in the axial location wave-number (X^*-n) space are provided in Figs. 21(a) and 21(b) for the primary and stationary modes. The primary mode is dominated by azimuthal components in the range of $n \in (0, 180)$ (for $\ln[K(n)] > -3$) up to $X^* \approx 390$ mm, beyond which the spectrum begins to fill up rapidly. The stationary mode also exhibits two distinct development phases in the streamwise direction. In the early stage, energy of the stationary mode mainly concentrates in the low azimuthal mode numbers ($n < 120$); additionally, a substantially smaller peak at $n \approx 700$ and its first harmonic at $n \approx 1400$ are also visible in the spectrum. The stationary mode enters into the late stage downstream of $X^* \approx 390$ mm where components in the vicinity of $n \approx 700$ are strongly enhanced, manifesting as multiple peaks in the spectrum; these peaks soon expand with almost constant spacings $\Delta n \approx 72$, covering almost the whole azimuthal wave-number region, and are eventually replaced by a more uniform distribution towards the outlet.
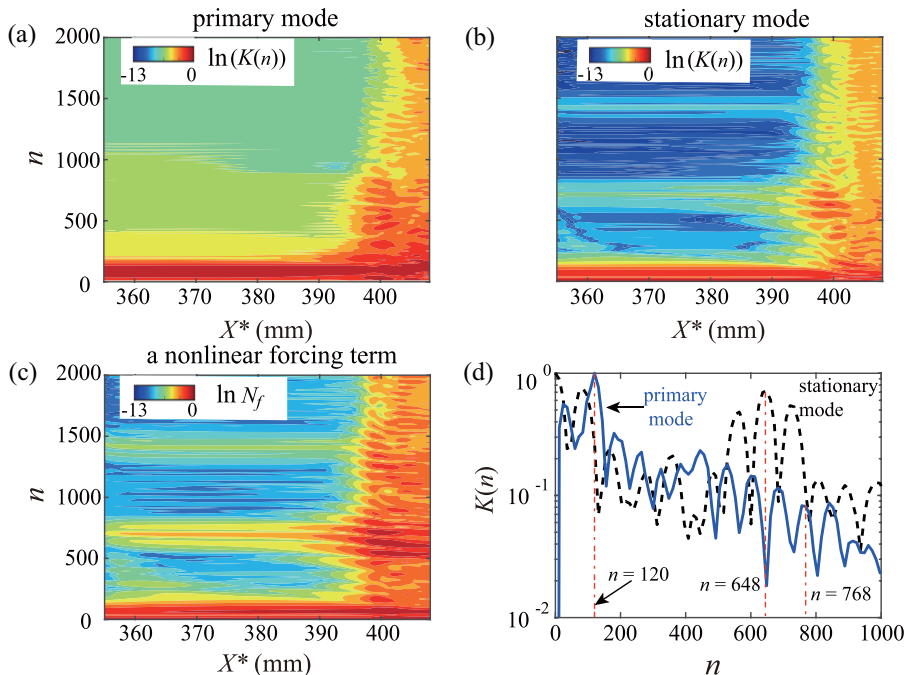
FIG. 21. Locally normalized amplitude spectra (in a logarithmic scale) in the X^*-n plane for (a) the primary mode, (b) the stationary mode, and (c) one of the main nonlinear forcing terms from the primary mode $N_f \equiv \max_\eta(\bar{\rho} u u^+)$. (d) Comparison of the normalized spectra of primary and stationary modes over the azimuthal wave number at $X^* = 400$ mm, with three peaks labeled forming a potential resonant triad.

It is interesting to note that in either the symmetric-mode case (see Fig. 16) or the antisymmetric-mode case, the rapid spectral broadening in the azimuthal wave number is initiated by an explosive burst of components in the vicinity of $n \approx 700$. Nevertheless, a qualitative difference between these two cases is still present during the "explosive-growth" stage, that is, the former case features a broadband rapidly growing components along with few harmonics, whereas the spectrum in the latter case exhibits many sharp peaks. This difference suggests another nonlinear mechanism than the fundamental resonance. A hint is given by Fig. 21(c) showing that the spectrum of one of the main nonlinear forcing terms $\bar{\rho} u u^+$ (u the streamwise velocity disturbance from the primary mode) in the streamwise momentum equation for the stationary mode is coincident with that of the stationary mode. This observation implies that the appearance and growth of the multiple peaks of the stationary mode are likely contributed by the interaction between different azimuthal components of the primary mode, as

$$(f^* = 1650 \text{ kHz}, n_2) - (f^* = 1650 \text{ kHz}, n_1) \rightarrow (f^* = 0, n_2 - n_1), \tag{23}$$

where n_1 and n_2 stand for the azimuthal wave numbers of two primary azimuthal components. In turn, the stationary component can also interact with one of the primary component to drive another primary component as

$$(f^* = 0, n_2 - n_1) + (f^* = 1650 \text{ kHz}, n_1) \rightarrow (f^* = 1650 \text{ kHz}, n_2). \tag{24}$$

The existence of such a triad interaction is evidenced by Fig. 21(d), which shows that stationary component (0,648) is very likely coupled with the dominant primary component (1650 kHz, 120) and the other primary component (1650 kHz, 768). The spatial development of the flow structures is shown in Fig. 22. The early-stage flow field is characterized by vortical structures at either side
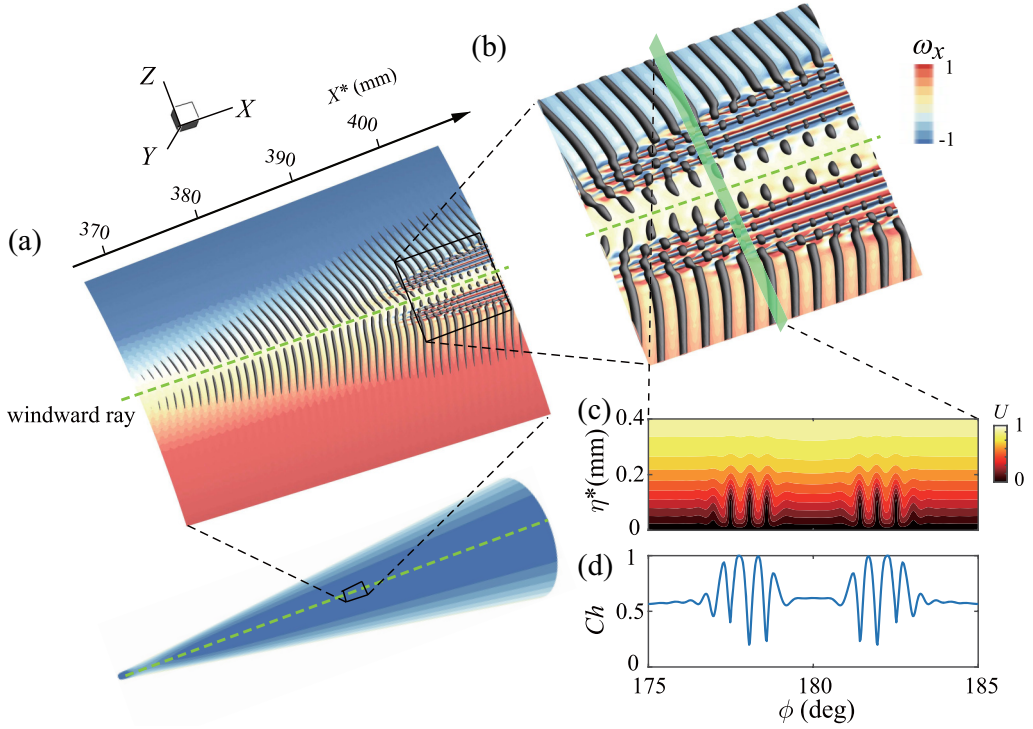
FIG. 22. Instantaneous flow pattern from NPSE3D calculations for the antisymmetric-mode case. (a) Vortical structures visualized by the isosurface of Q criterion ($Q = 0.1$), along with isosurface of axial velocity ($U = 0.2$) colored by normalized axis vorticity (ω_x). (b) Zoomed-in image of the spatial structure corresponding to the squared region in (a). (c) The normalized axial velocity in the cross section at the middle of the region ($X^* = 400$ mm) in (b). (d) The normalized Stanton number distribution in the azimuthal direction.

of the windward ray that are inclined in the opposite direction with respect to that of the base flow. Far downstream, the vortical structures close to the windward ray break up due to the emergence of strong streamwise vorticities with alternating sign. Between the adjacent streamwise vorticities arise the low- and high-speed thermal streaks. The appearance of the longitudinal structures is attributed to the amplifying stationary mode. Since the streak structures lie a certain distance away from the windward ray, it is interesting to examine whether the structures of either side of the windward ray will interact with each other in nonlinear development of the antisymmetric mode. In order to remedy such possibility of interactions, we adopt Dirichlet boundary conditions (i.e., all variables vanish) at the windward ray, and recalculate the NPSE3D with nominally the same conditions. The results are shown in Fig. 20(a). Obviously, the nonlinear development of the mode amplitude is almost unaffected by the boundary conditions, indicating that the disturbances on either side appear to evolve independently.

3. Energy transfer analysis

In an attempt to understand the underlying mechanisms of the rapid growth of the stationary mode during the secondary-instability stage, we consider the total energy transfer equation for one mode as

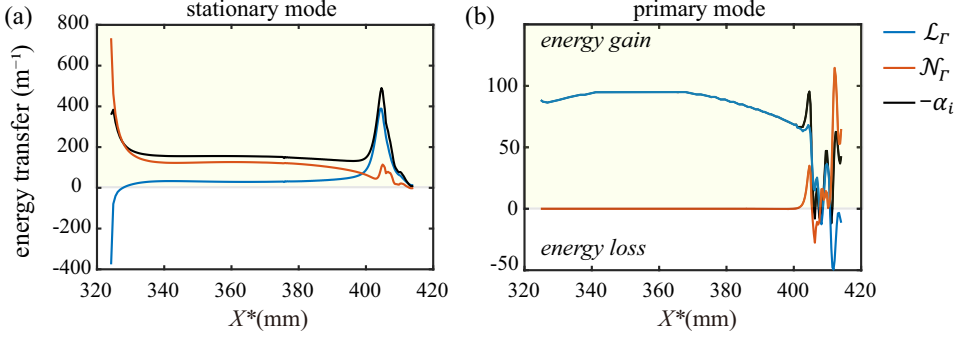$$\frac{1}{2}\frac{DE}{Dt} = \mathcal{L}_e + \mathcal{N}_e, \tag{25}$$

FIG. 23. Linear and nonlinear energy transfers for (a) the stationary mode and (b) the primary mode. The growth rates are included for reference.

where E represents the total disturbance energy [60]

$$E = \frac{\bar{T}}{\bar{\rho}\gamma M^2}|\rho'|^2 + \bar{\rho}(|U'|^2 + |V'|^2 + |W'|^2) + \frac{\bar{\rho}|T'|^2}{\gamma(\gamma-1)M^2\bar{T}};\quad (26)$$

$\mathcal{L}_e$ quantifies the energy exchanged per unit volume between the mode itself and the undisturbed mean flow, as well as dilatation and viscous dissipation. $\mathcal{L}_e$ is directly caused by linear terms although nonlinear forces exert an indirect influence on the energy exchange through changing the mode shapes or the disturbance amplitudes. $\mathcal{N}_e$ represents the energy variation caused by nonlinear terms. The derivation of Eq. (25) can be found in Appendix E. Unlike the incompressible case (see, for example, [61,62]) where $\mathcal{N}_e$ only consists of disturbance variables and is thus interpreted as the energy exchange between disturbance modes, $\mathcal{N}_e$ here contains the mean-flow variables and as such transfers energy from/to mean flow as well as other modes.

Equation (25) can be integrated over the cross-section plane Ω and divided by

$$\Gamma = \int \bar{\rho}\bar{U}\left[\frac{\bar{T}}{\bar{\rho}^2\gamma M^2}|\hat{\rho}|^2 + |\hat{U}|^2 + |\hat{V}|^2 + |\hat{W}|^2 + \frac{|\hat{T}|^2}{\gamma(\gamma-1)M^2\bar{T}}\right]\exp\left(-2\int\alpha_i d\xi\right)d\Omega \quad (27)$$

to give

$$-\alpha_i = \mathcal{L}_\Gamma + \mathcal{N}_\Gamma, \quad (28)$$

where

$$\mathcal{L}_\Gamma = \int \mathcal{L}_e d\Omega/\Gamma, \quad \mathcal{N}_\Gamma = \int \mathcal{N}_e d\Omega/\Gamma. \quad (29)$$

$\mathcal{L}_\Gamma$ and $\mathcal{N}_\Gamma$ represent the growth rates contributed by the linear and nonlinear terms, respectively. Because results of the energy transfer analysis for the symmetric-mode case and the antisymmetric-mode case turn out to be similar, we only present results for the symmetric-mode case here. The streamwise development of the integrated linear and nonlinear energy transfers of the stationary mode and the primary mode is plotted in Fig. 23. For the stationary mode, the nonlinear energy transfer drops sharply in the beginning, whereas the linear energy transfer increases steeply from a negative value to a small positive one. Such rapid changes in the energy transfers correspond to the transient growth process of the stationary mode, as evidenced by the initial algebraiclike growth in the amplitude evolution [see, for example, Fig. 14(a)]. Physically, the transient growth is contributed primarily by the energy gain of the streamwise velocity perturbation via the liftup effect induced by streamwise vorticity components comprising of transverse velocities [63,64]. The transient growth process can also be inferred from Fig. 24(a) showing that the ratio of the transverse velocity magnitude to the streamwise one quickly decreases from 0.5 to about 0.1. As
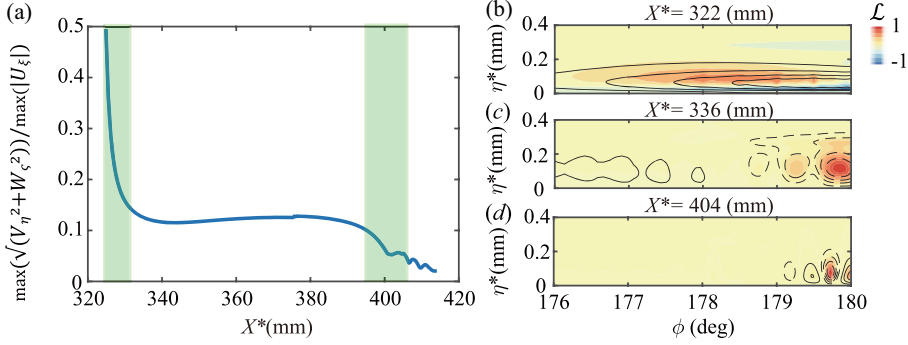
FIG. 24. (a) Streamwise development of the ratio of the transverse velocity magnitude to the streamwise velocity magnitude for the stationary mode. The rapid decrease of this ratio in the initial and final stages (marked by the filled regions) suggests presence of the transient growth. Linear energy transfer distribution at three presentative axial stations, i.e., (b) $X^* = 322$ mm (inlet), (c) $X^* = 336$ mm (end of the initial transient stage), and (d) $X^* = 404$ mm (peak location of energy transfers), together with the streamwise velocity disturbance isolines (solid lines denote positive values and dashed lines negative values).

a consequence, prominent azimuthal variations manifest themselves in the streamwise velocity perturbation towards the end of the transient-growth stage [see Figs. 24(b) and 24(c)].

In the downstream region, the nonlinear energy transfer is still dominant and varies slowly, while the linear energy transfer remains at a small, yet positive, value. For $X^* > 395$ mm, the linear energy transfer starts to rise steeply, surpassing the nonlinear energy transfer and peaking at $X^* \approx 404$ mm; on the other hand, the nonlinear energy transfer first decreases, then slightly increases before decaying again. Such an appreciable enhancement of the linear energy transfer is attributed to the secondary instability, and is involved in the formation process of the streaks where the liftup mechanism may again have played an important role as inferred from Figs. 24(a) and 24(d). The results clearly show that the secondary-instability growth of the stationary mode is sustained primarily by the linear energy transfer, that is, the primary mode acts as a catalyst, allowing the mean flow to transfer energy to the stationary mode. For the primary mode, the linear energy transfer is always dominant while the nonlinear energy transfer is inactive preceding the secondary-instability stage, as illustrated in Fig. 23(b). Slightly downstream of the secondary-instability onset of the stationary mode, both the linear and nonlinear energy transfers first undergo a rapid growth, also peaking at $X^* = 404$ mm, then quickly drop and oscillate around the zero value. Contrary to the stationary mode whose components in the azimuthal wave-number space are basically amplifying in the secondary-instability stage, the primary mode components with low azimuthal wave numbers are decaying as inferred from Fig. 15 so that the energy transfers during the secondary-instability stage are not as prominently amplified as those of the stationary mode. As shown above, the linear energy transfer plays a significant role in the secondary-instability stage, and thus necessitates a further assessment. Following the work of Chen *et al.* [13,65], the linear energy transfer can be conveniently divided into four parts as

$$\mathcal{L}_e = \mathcal{P} + \Pi + \mathcal{V} + \mathcal{C}. \tag{30}$$

The production reads as

$$\mathcal{P} = -\text{Real}\left[\underbrace{\bar{\rho} U_\xi'^\dagger u_j' \frac{\partial \bar{U}_\xi}{\partial x_j}}_{\mathcal{P}^U} + \underbrace{\frac{\bar{\rho}}{\gamma(\gamma-1)M^2\bar{T}} T'^\dagger u_i' \frac{\partial \bar{T}}{\partial x_i}}_{\mathcal{P}^T} + \underbrace{\frac{\bar{T}}{\gamma M^2 \bar{\rho}} \rho'^\dagger u_i' \frac{\partial \bar{\rho}}{\partial x_i}}_{\mathcal{P}^\rho} \right],$$

$$u_i \equiv [U_\xi, V_\eta, W_\zeta], \, x_i \equiv [\xi, \eta, \zeta] \tag{31}$$
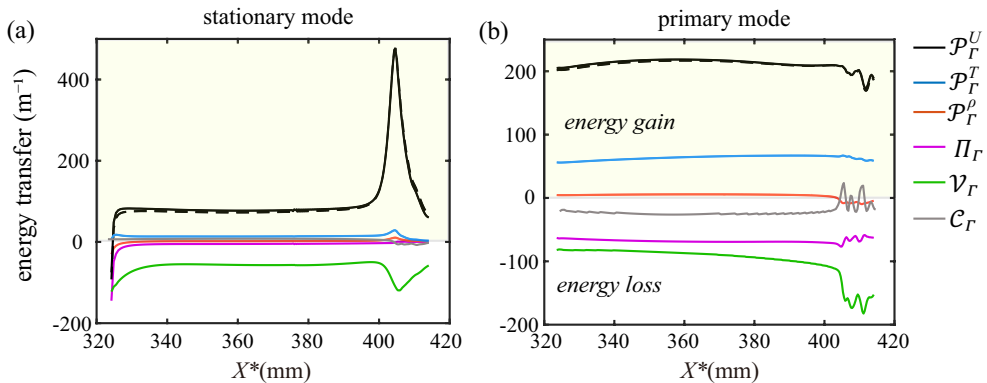
FIG. 25. Linear energy budget for (a) the stationary mode and (b) the primary mode. The dashed line represents the production term pertaining to the wall-normal shear of the streamwise velocity.

representing the energy transfer from the mean flow to the disturbance. Note that the production contains three parts, i.e., the Reynolds stress work ($\mathcal{P}^U$), the energy transfer owing to the temperature gradient ($\mathcal{P}^T$), and the energy transfer owing to the density gradient ($\mathcal{P}^\rho$). $\Pi = -u_i'^\dagger \frac{\partial P'}{\partial x_i} + \text{c.c.}$ denotes the pressure diffusion and dilatation, $\mathcal{V}$ (too lengthy to be shown here) is the energy transfer associated with the viscous terms, and $\mathcal{C}$ represents the remainder terms.

The contribution of each of these terms to the growth rates of the stationary and primary modes is displayed as a function of axial locations in Fig. 25. Obviously, the production term associated with the wall-normal shear of the streamwise velocity $-\bar{\rho} U_\xi'^\dagger V_\eta' \partial \bar{U}_\xi / \partial \eta$ is predominant for both modes, substantially larger than the production from the temperature and density gradients. This indicates that the disturbance energy mainly comes from the wall-normal shear of the mean flow extracted by the Reynolds stress. In contrast, the linear energy transfers pertaining to the pressure and viscous terms are always negative, indicating the disturbance energy loss.

D. Streak instabilities in the late nonlinear stage

Finally, we attempt to describe, approximately, the stability characteristics of the late-stage flow field. In the late stage of the nonlinear development of either the symmetric- or antisymmetric-mode case, the amplitude of the stationary mode, changing slowly, is nearly one order of magnitude larger than that of the primary mode as inferred from Figs. 14 and 20. Therefore, we can reasonably neglect the unsteady modes and formulate a quasi-steady-streak stability problem that is solved by the BiGlobal approach. Significantly unstable modes of the streaky structures in the symmetric-mode case and the antisymmetric-mode case are shown in Fig. 26. For the symmetric-mode case, mode 1 is dominant with a peak frequency at 150 kHz and almost exclusively resides in the double-streak structure of the base flow. In analogy with the streak instability with spanwise periodicity [45,66], mode 1 can be viewed as a subharmonic sinuous mode. Similarly, streaks in the antisymmetric-mode case support several unstable modes in the frequency range of (50,300) kHz and the most unstable mode is also analogous to a subharmonic sinuous mode. Tests (not shown here) indicate that the streak instabilities in both cases are slightly stabilized further downstream due to the slow attenuation of streaks, but the peak frequencies do not change much so that the integrated amplification rates are still considerable.

IV. CONCLUDING REMARKS

A comprehensive study is presented of the Mack-mode instability on the windward face of a hypersonic yawed blunt cone at a flight condition, focusing on global linear instability characteristics
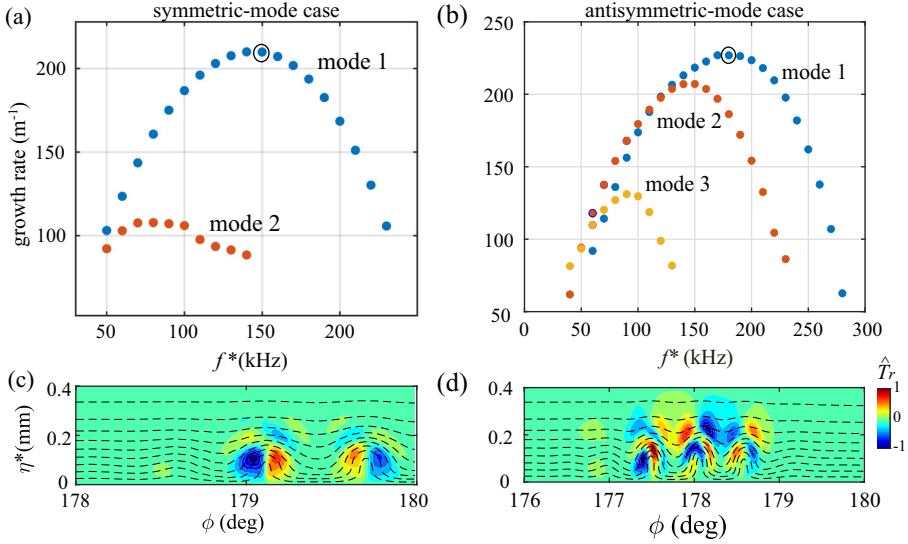
FIG. 26. Stability characteristics for the streak structure in the symmetric-mode case at $X^* = 407$ mm (a), (c) and for the streak structure in the antisymmetric-mode case at $X^* = 400$ mm (b), (d). (a), (b) Growth rates as a function of frequency, with the most amplified frequency being marked by circles. (c), (d) Real parts of the normalized temperature shape function of the most unstable mode of each case. The base flow depicted by the axial velocity is shown for reference (dashed lines).

and nonlinear instability mechanisms. The important findings are summarized in Fig. 27, sketching the potential windward transition scenario.

A. Linear instability mechanisms

The high-frequency (MHz) Mack-mode instability and low-frequency ($\lhd 00$ kHz) crossflow instability are present in the windward side, of which the former dominates. The global eigenvalue spectrum of the Mack-mode instability reveals the coexistence of two distinct branches of modes: branch S is composed of a sequence of wave-packet modes lying in a certain distance away from the windward ray, resembling the oblique Mack-mode instabilities identified in other crossflow-dominated configurations [20,53]; branch D, splitting from branch S and analogous to the attachment-line instability, consists of few discrete modes concentrating in the vicinity of the windward ray. The integrated growth rates of the D modes are sufficiently large to potentially trigger the transition. The S modes are less amplified and unlikely trigger the transition in their occupying region, but they probably excite the D modes when propagating downstream. In other words, Mack-mode transition will first occur in the vicinity of the windward ray, in accord with the indented transition front observed in the flight test [24].

B. Weakly nonlinear transition mechanisms

Nonlinear instability of the finite-amplitude leading symmetric D mode is studied with a combination of one-dimensional approaches (NPSE2D and Floquet analysis) as well as the global approach (NPSE3D). It is demonstrated that a single global Mack mode could break down by itself through fundamental resonances before saturating. This differs in nature from axisymmetric configurations where a single Mack mode can not principally break down without seeding any additional disturbances. This is because the global Mack mode inherently contains fundamental oblique components with a wide range of azimuthal wave numbers, and thereby simultaneously
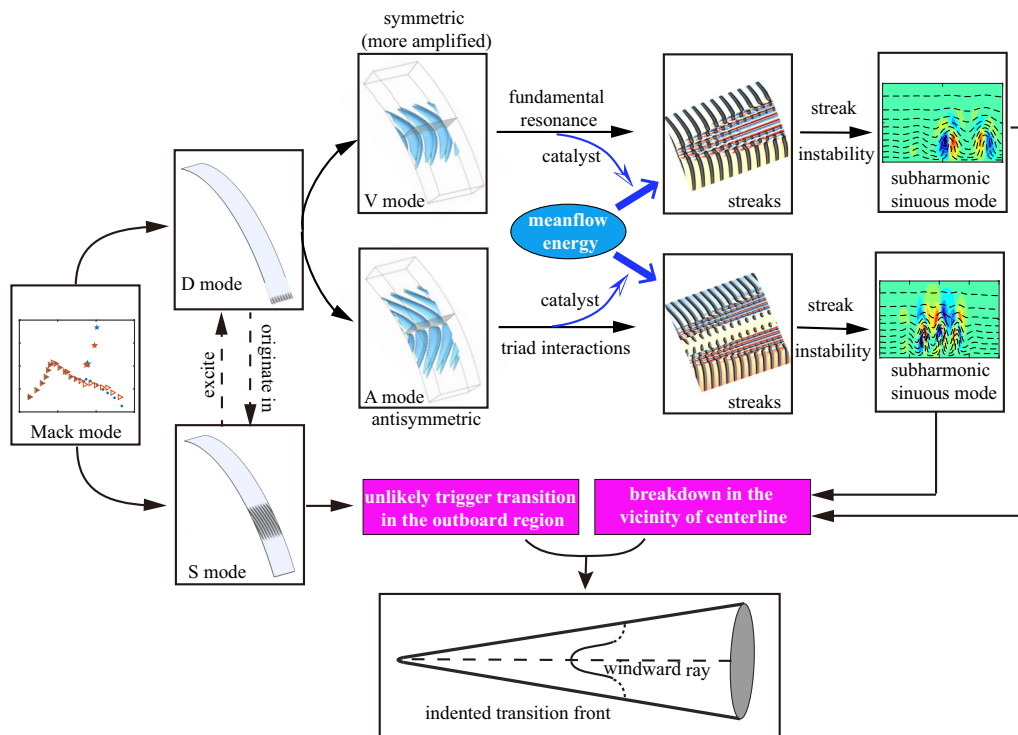
FIG. 27. Sketch of the relevant windward transition scenario identified in this study for an inclined blunt cone at a flight condition.

generates stationary components. The fundamental oblique and stationary components with certain azimuthal wave numbers will subsequently be largely promoted due to the fundamental resonance. The resulting flow pattern features streaky structures in the vicinity of the windward ray, much akin to that of a nonlinear Mack-mode wave packet in an axisymmetric flared-cone boundary layer [14]. The dominant azimuthal wave number is around 600, which is substantially higher than the prevailing azimuthal wave numbers ($40 < n < 150$) of the fundamental resonance in axisymmetric configurations studied before [13,59,67]. Nevertheless, the wave angle Ψ_f of the strongest fundamental secondary wave in this study is around $32°$, which is still in the range of the dominant wave angles, i.e., $30° < \Psi_f < 50°$, documented in the previous studies. This indicates that the wave angle is a more universal feature that characterizes the fundamental resonance than the azimuthal wave number. Interestingly, the maximum secondary-instability growth rates are found to be as large as 1600 m^{-1}, almost 10 times larger than those reported by the previous studies for axisymmetric configurations (see, for example, [12,13,36]). As a result, the Mack-mode wave is deemed to break down immediately at onset of secondary instability. Furthermore, the combination resonance, likely arising from side-band interactions between Mack modes with different frequencies, is shown to be inevitably accompanied by and dominated by the fundamental resonance in the global context.

Nonlinear development of the leading antisymmetric D mode is also investigated via NPSE3D. This mode manifests as a pair of nearly straight structures inclined at opposite directions at two sides of the windward ray. The fundamental resonance is inactive due to absence of the planar component, yet interactions between components of different azimuthal wave numbers can still yield a rapid spectral-broadening process in the azimuthal wave-number space. Coincidentally, the most amplified azimuthal wave numbers in the early nonlinear stage are close to those of the fundamental resonance in the symmetric-mode case. The underlying mechanism of the preferential

wave numbers needs a further exploration. In the late stage, streaky structures also emerge and dominate the flow field.

Energy transfer analysis shows that the global Mack mode acts like a catalyst, remarkably enhancing the ability of the stationary mode to extract energy from the mean flow. Such an energy transfer, where the liftup effect presumably plays an important role, is responsible for the amplification of the stationary mode, giving birth to streaks. The catalytic role played by the primary mode in the parametric-instability stage has been frequently documented in two-dimensional cases [10,58], and is confirmed by this study in a truly three-dimensional configuration.

The streak instability in the late stage of both the symmetric- and antisymmetric-mode cases is analyzed by BiGlobal. The results indicate that low-frequency (≲300 kHz) disturbances of subharmonic sinuous type are highly unstable and are likely responsible for the final breakdown. Since the symmetric D mode is more unstable than the antisymmetric counterpart, fundamental breakdown is the most relevant transition scenario in the vicinity of the windward ray. Nevertheless, the transition scenario initiated by the antisymmetric mode is still of great significance as it is a representative of those in the crossflow region far away from the symmetry planes where global modes (Mack modes or crossflow modes), disregarding the symmetry characteristic, exhibit qualitatively the same modal structures as the antisymmetric D mode. Moreover, oblique breakdown is not observed for both cases because on either side of the windward ray, the mode consists exclusively of components with wave angles of the same sign, prohibiting interactions between components with opposite wave angles.

At last, it is helpful to discuss the sensitivity of the main findings to the initial conditions since the initial phases of different modes are random in space and time in natural transition. Our results indicate that the transition scenario featured by the fundamental resonance and the ensuing streak breakdown is robust to variations of the frequency and initial amplitude of the dominating wave (Appendix D), and also holds true in the presence of side-band interactions between two modes with arbitrarily initial phases (Sec. III C 2) or even more complicated interactions as studied by Yang. [28] on the evolution of a nonlinear wave packet. Nevertheless, some quantitative properties such as the breakdown location and the dominating spacings of the streaks are expected to change with varying initial conditions.

C. Future work

In order to verify the theoretical results above (and further investigate the transition process) by direct numerical simulations, we need to conduct a DNS with an extremely large number of grid points in the streamwise direction (to capture the Mack-mode wave and its harmonics) as well as in the azimuthal direction (to capture the streak structures with rather small spacings), which is, however, beyond our current ability. Nevertheless, preliminary comparison (Appendix C) of the DNS results [27] and the present theoretical results shows a promising agreement. Work in this direction is under way.

APPENDIX A: VERIFICATION OF NPSE3D

Two types of modal interactions listed in Table III were separately calculated by NPSE2D and NPSE3D for a hypersonic flat-plate boundary layer. Case K corresponds to the fundamental-

TABLE III. Initially seeded modes of NPSE for a flat-plate boundary layer under flow conditions of Mach 6, $T_\infty^* = 48.8$ K, and the stagnation wall condition. The initial amplitude is measured in terms of the peak temperature fluctuation.

Case	Planar mode and initial amplitude	Oblique mode and initial amplitude	Frequency ($F \times 10^6$)	Spanwise wave number (β)
K	(1,0), 1%	(1,1), 0.1%	111	0.05
O		(1,1), 1%	111	0.05

breakdown-type interaction, while case O is associated with the oblique breakdown. For NPSE3D, the spanwise length of the computational domain is $2\pi/\beta$, corresponding to a single wavelength of the primary oblique mode. The spanwise direction is discretized by 20 Fourier collocation points. The results are presented in Fig. 28. Obviously, results from two methodologies almost coincide for both cases, hence verifying the NPSE3D code.

APPENDIX B: GRID CONVERGENCE FOR GLOBAL STABILITY ANALYSIS

For the purpose of examining the grid convergence of the BiGlobal results for Mack-mode instabilities, calculations of eigenvalue spectra were performed with three grid resolutions in both azimuthal and wall-normal directions, and the results are compared in Fig. 29. Given that continuous-type global modes in three-dimensional boundary layers are very sensitive to the azimuthal resolutions [20,53], the results are deemed converged for 600 azimuthal grid points in the sense that the peak growth rates, peak phase velocity, and the spectrum pattern remain unchanged. In contrast, the global modes are relatively insensitive to the wall-normal resolution, and the results with 101 wall-normal grid points are already satisfying. Next, we examine the grid convergence of NPSE3D by comparing the amplitude evolutions of test cases in Table IV. Note that the grids in the azimuthal direction of all cases are stretched so that at least 50 points are put within [178°, 180°]. The results are displayed in Fig. 30, showing a good convergence even for the coarsest grid. The fundamental resonance and the subsequent saturation state are observed for all the cases, albeit slight movements of onset locations of the fundamental resonance.

APPENDIX C: COMPARISON WITH DNS RESULTS BY YANG

Yang [27] carried out direct numerical simulations to investigate the nonlinear development of a single-frequency Mack-mode wave for the same flow configuration as in this study. Below we will
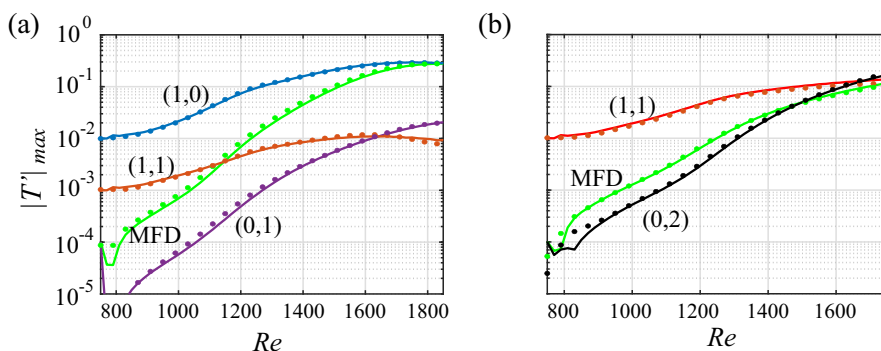

FIG. 28. Comparison of NPSE2D and NPSE3D results for the amplitude evolution of representative modes in case K (a) and case O (b) with conditions being summarized in Table III.
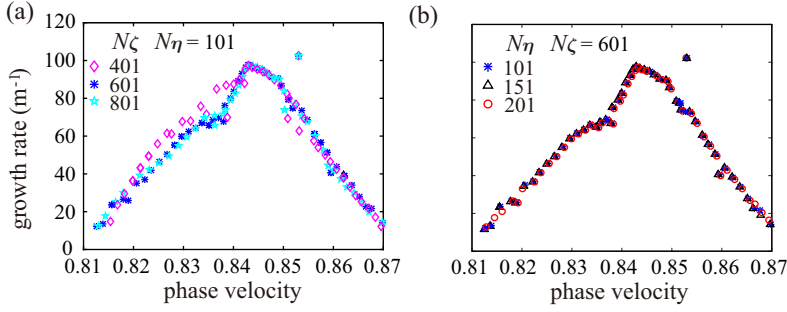
FIG. 29. Convergence test of BiGlobal for global modes with frequency of 1560 kHz at $X^* = 400$ mm: (a) grid convergence in the azimuthal direction, (b) grid convergence in the wall-normal direction.

briefly introduce some important DNS results and make a comparison with the present theoretical results where possible.

In the DNS, the fluctuations were introduced by the azimuthally uniform unsteady blowing and suction as

$$v_{bs} = \mathcal{A}_v \sin[(X^* - X_1^*)/(X_2^* - X_1^*)]^3 \cos(2\pi f^* t^*), \tag{C1}$$

where $\mathcal{A}_v$ is the amplitude of the wall-normal velocity equal to 0.1% U_∞^*, $X_1^* = 280$ mm, $X_2^* = 282$ mm, and $f^* = 1750$ kHz. The grid resolution is $N_\xi \times N_\zeta \times N_\eta = 8100$ (axial direction) $\times$ 240 (azimuthal direction) $\times$ 380 (wall-normal direction), amounting to a total of 0.74×10^{11} grid points. In the range of interest $X^* \in (250, 550)$ mm, the axial grid distribution is uniform and denser than the upstream and downstream regions, ensuring approximately 18 points for each axial wavelength of the Mack-mode wave at frequency 1750 kHz. Most of the azimuthal grid points are uniformly distributed in the windward side [$\phi \in (90, 270)°$] so that the azimuthal spacing between adjacent points is approximately $1°$. Seventh-order weighted essentially nonoscillatory (WENO) finite-difference scheme and sixth-order central difference scheme were utilized for discretizing the convective and viscous terms, respectively. Figure 31 presents the normalized temperature root mean square (rms) at four successive stations. Although planar perturbations were excited through the blowing and suction, the temperature rms at the first station already exhibits a prominent concentration on the windward ray. Further downstream, the outboard disturbance continues to weaken compared to that in the vicinity of the windward ray so that the temperature rms at the third station appears to be restricted within about $\pm 3°$ with respect to the windward ray. This is consistent with the global analysis results of this study that perturbations in the proximity of the windward line will eventually prevail. At the last station, additional rms peaks emerge at the two sides of the primary one, which is possibly attributed to the growth of broad-band disturbances as will be shown later. The above results indicate that the spatial development of Mack-mode instability in the windward side is dominated by the branch D mode at least up to the late stage. This is further evidenced by Fig. 32, which displays the amplitude developments of the wall pressure disturbances along the windward ray separately extracted from the primary frequency (1750 kHz) and all the

TABLE IV. Convergence test of NPSE3D for the symmetric-mode case.

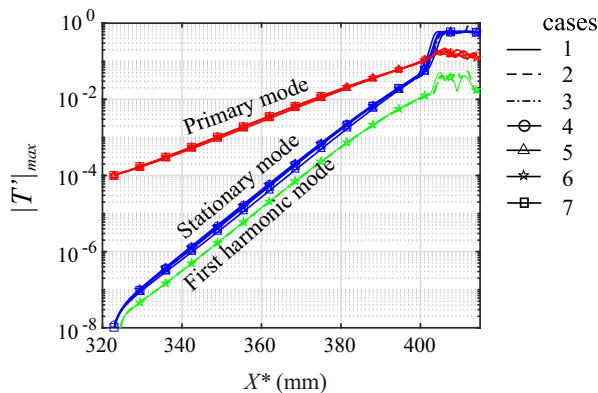| Case	1	2	3	4	5	6	7
N_ζ	200	200	200	100	250	300	150
N_η	100	100	100	100	150	100	100
Modes included	2	3	4	2	2	3	2
Azimuthal domain	168°–180°	168°–180°	168°–180°	168°–180°	162°–180°	168°–180°	150°–180°

FIG. 30. Convergence test of NPSE3D for cases listed in Table IV. Only the first three modes in each case are displayed.

frequencies. It can be seen that the disturbance amplitude undergoes an exponential growth, peaks at approximately $X^* = 375$ mm and subsequently decays. For comparison, we further performed LPSE3D and NPSE3D calculations initiated by the branch D mode at frequency 1750 kHz. In NPSE3D, the initial amplitude is prescribed to be the same as the DNS results at $X^* = 300$ mm. Obviously, the LPSE3D results adequately capture the exponential-growth stage, while the NPSE3D results faithfully predict the saturation and decay phases. The peak temperature disturbance amplitude of the primary frequency estimated from NPSE3D results is about 6%, much smaller than the fundamental resonance threshold (10%) given by the theoretical results above, hence the primary disturbance is unlikely to trigger the laminar boundary-layer breakdown. This is supported by the DNS results that the fundamental disturbance amplitude decay all the way to the initial amplitude level. Interestingly, DNS results show that disturbances from other frequencies, possibly originating in numerical noise, manifest and dominate the flow field downstream of $X^* > 440$ mm.
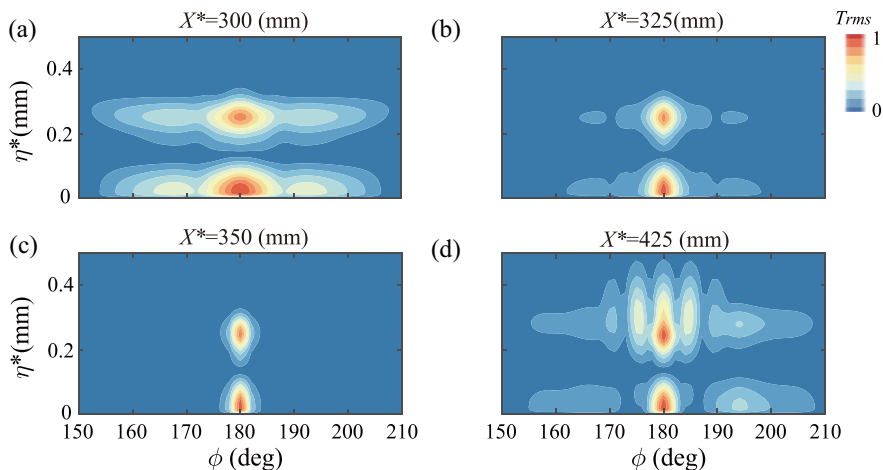

FIG. 31. Distribution of the normalized root-mean-square (rms) of the temperature disturbance in the cross sections of selected axial stations, obtained from the first DNS case. (a) $X^* = 300$ mm, (b) $X^* = 325$ mm, (c) $X^* = 350$ mm, (d) $X^* = 425$ mm. Reproduced from [27], Fig. 4.4.
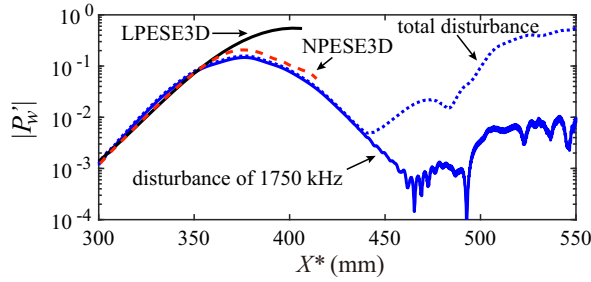
FIG. 32. Downstream development of the pressure disturbance amplitude of 1750 kHz (blue solid line) and the total disturbance amplitude (dotted line) extracted at the wall along the windward ray from the first DNS case. The pressure disturbance is normalized by the free-stream pressure. Reproduced from Yang [27], Fig. 4.3. The LPESE3D results (black solid line) and the NPSE3D results (red dashed line) with the same initial amplitude calculated by this study are also displayed for comparison.

APPENDIX D: PARAMETRIC EFFECTS ON THE NONLINEAR DEVELOPMENT OF THE D MODE

In this Appendix, we examine whether the fundamental resonance is robust under various conditions. Figure 33(a) compares the amplitude evolutions in cases with different initial amplitudes. It can be seen that the fundamental resonance manifests itself for cases whenever the primary mode amplitude exceeds about 10% for the temperature disturbance (3.7% for the mass-flow disturbance or 0.8% for the pressure disturbance). Increasing the initial amplitude leads to the forward movement of the onset of the fundamental resonance as well as the saturation location, but does not change the growth rates (estimated by the slope of the amplitude curve). Figure 33(b) displays the frequency effects on the fundamental resonance. Each frequency features a different initial amplitude in order to separate the curves for better visual clarity. Again, the fundamental resonance is visible for all the three primary frequencies once the primary mode amplitude exceeds about 10%. Moreover, the growth rates of the stationary mode in the fundamental-resonance stage seem to slightly decrease with increasing frequency.
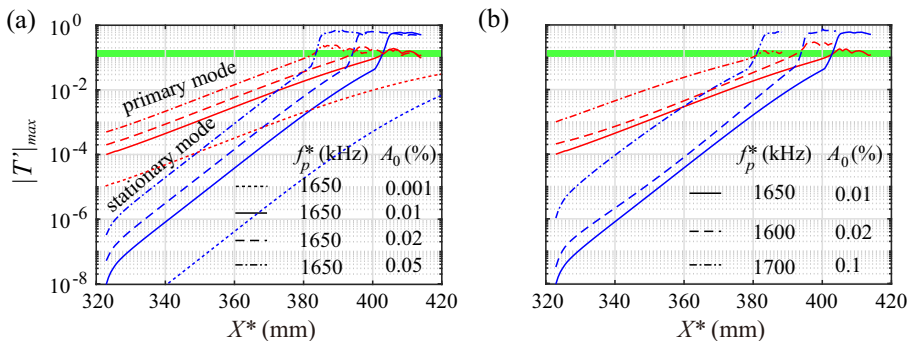

FIG. 33. Parametric effects on the fundamental resonance. (a) Effects of initial amplitudes (A_0) of the primary mode. (b) Effects of the frequency (f_p^*) of the primary mode. The thick green line denotes the amplitude threshold (10%).

APPENDIX E: ENERGY TRANSFER

An energy balance equation can be derived by considering the perturbation equations (14). The streamwise momentum equation for one mode (with frequency mF) can be expressed as

$$\bar{\rho}\frac{\mathrm{D}U_\xi'}{\mathrm{D}t} = -\mathcal{L}_u\boldsymbol{q}' + \mathcal{N}_u, \tag{E1}$$

where $\mathcal{L}_u$ denotes the linear operator; $\mathcal{N}_u$ quantifies the nonlinear forcing; $\mathcal{D}/\mathcal{D}t \equiv \partial/\partial t + \bar{U}_\xi\partial/\partial\xi$. The subscript (m) has been omitted for simplicity. Multiply Eq. (E1) by $U_\xi'^\dagger$ (the complex conjugate of U_ξ'), multiply the complex conjugate of Eq. (E1) by U_ξ', and then add these two equations to get

$$\bar{\rho}\frac{\mathrm{D}|U_\xi'|^2}{\mathrm{D}t} \equiv -2\alpha_i\bar{\rho}\bar{U}_\xi|\hat{U}_\xi|^2\exp\left(-2\int\alpha_i d\xi\right) = -U_\xi'^\dagger\mathcal{L}_u\boldsymbol{q}' + U_\xi'^\dagger\mathcal{N}_u + \text{c.c.}, \tag{E2}$$

where the PSE3D assumption (13) has been adopted. By applying similar operations to the momentum equations in other two directions, the continuity equation and the energy equation, we obtain the total disturbance energy transport equation

$$\frac{1}{2}\bar{\rho}\frac{\mathrm{D}E}{\mathrm{D}t} \equiv -\alpha_i\bar{\rho}|\bar{U}_\xi|\left(|\hat{U}_\xi|^2 + |\hat{V}_\eta|^2 + |\hat{W}_\zeta|^2 + \frac{\bar{T}}{\bar{\rho}^2\gamma M^2}|\hat{\rho}|^2 + \frac{|\hat{T}|^2}{\gamma(\gamma-1)M^2\bar{T}}\right)$$
$$\times\exp\left(-2\int\alpha_i d\xi\right) = \mathcal{L}_e + \mathcal{N}_e, \tag{E3}$$

where

$$\mathcal{L}_e \equiv -\tfrac{1}{2}(U_\xi'^\dagger\mathcal{L}_u\boldsymbol{q}' + V_\eta'^\dagger\mathcal{L}_v\boldsymbol{q}' + W_\zeta'^\dagger\mathcal{L}_w\boldsymbol{q}' + \rho'^\dagger\mathcal{L}_c\boldsymbol{q}' + T'^\dagger\mathcal{L}_T\boldsymbol{q}' + \text{c.c.}) \tag{E4}$$

and

$$\mathcal{N}_e \equiv \tfrac{1}{2}(U_\xi'^\dagger\mathcal{N}_u\boldsymbol{q}' + V_\eta'^\dagger\mathcal{N}_v\boldsymbol{q}' + W_\zeta'^\dagger\mathcal{N}_w\boldsymbol{q}' + \rho'^\dagger\mathcal{N}_c\boldsymbol{q}' + T'^\dagger\mathcal{N}_T\boldsymbol{q}' + \text{c.c.}). \tag{E5}$$

[1] L. Lees and C.C. Lin, Investigation of the stability of the laminar boundary layer in a compressible fluid, NASA Technical Report No. 1115 (unpublished).

[2] L. M. Mack, Boundary-layer linear stability theory, in *AGARD-R-709 Special Course on Stability and Transition of Laminar Flow* (AGARD, 1984), pp. 1–81.

[3] P. Balakumar and H. Reed, Stability of three-dimensional supersonic boundary layers, Phys. Fluids A **3**, 617 (1991).

[4] F. Li, M. Choudhari, C.-L. Chang, J. White, R. Kimmel, D. Adamczak, M. Borg, S. Stanfield, and M. Smith, Stability analysis for HIFiRE experiments, in *Proceedings of the 42nd AIAA Fluid Dynamics Conference and Exhibit* (AIAA, Reston, VA, 2012), paper AIAA 2012-2961.

[5] E. Perez, H. Reed, and J. Kuehl, Instabilities on a hypersonic yawed straight cone, in *Proceedings of the 43rd Fluid Dynamics Conference* (AIAA, Reston, VA, 2013), paper AIAA 2013-2879.

[6] M. W. Tufts and R. L. Kimmel, Analysis of windward side hypersonic boundary layer transition on blunted cones at angle of attack, in *Proceedings of the 55th AIAA Aerospace Sciences Meeting* (AIAA, Reston, VA, 2017), paper AIAA 2017-0764.

[7] B. Wan, G. Tu, X. Yuan, J. Chen, and Y. Zhang, Identification of traveling crossflow waves under real hypersonic flight conditions, Phys. Fluids **33**, 044110 (2021).

[8] P. Paredes, A. Scholten, M. Choudhari, and F. Li, Hypersonic boundary-layer transition on blunted cones at angle of attack, in *Proceedings of the AIAA Aviation 2021 Forum* (AIAA, Reston, VA, 2021), paper AIAA 2021-2886.

[9] P. Paredes, V. Theofilis, and H. L. Reed, High-frequency instabilities along the windward face of a hypersonic yawed circular cone, in *Proceedings of the 7th AIAA Theoretical Fluid Mechanics Conference* (AIAA, Reston, VA, 2014), paper AIAA 2014-2774.

[10] Th. Herbert, Secondary instability of boundary layers, Annu. Rev. Fluid Mech. **20**, 487 (1988).

[11] Y. S. Kachanov, Physical mechanisms of laminar-boundary-layer transition, Annu. Rev. Fluid Mech. **26**, 411 (1994).

[12] F. Li, M. Choudhari, C.-L. Chang, and J. White, Analysis of instabilities in non-axisymmetric hypersonic boundary layers over cones, in *Proceedings of the 10th AIAA/ASME Joint Thermophysics and Heat Transfer Conference* (AIAA, Reston, VA, 2010), paper AIAA 2010-4643.

[13] X. Chen, Y. Zhu, and C. Lee, Interactions between second mode and low-frequency waves in a hypersonic boundary layer, J. Fluid Mech. **820**, 693 (2017).

[14] C. Hader and H. F. Fasel, Three-dimensional wave packet in a Mach 6 boundary layer on a flared cone, J. Fluid Mech. **885**, R3 (2020).

[15] F. Li, M. Choudhari, C.-L. Chang, R. Kimmel, D. Adamczak, and M. Smith, Transition analysis for the HIFiRE-1 flight experiment, in *Proceedings of the 41st AIAA Fluid Dynamics Conference and Exhibit* (AIAA, Reston, VA, 2011), paper AIAA 2011-3414.

[16] A. B. Hartman, C. Hader, and H. F. Fasel, Nonlinear transition mechanism on a blunt cone at Mach 6: oblique breakdown, J. Fluid Mech. **915**, R2 (2021).

[17] X. Chen, D. Xu, and S. Fu, Oblique-mode breakdown in hypersonic and high-enthalpy boundary layers over a blunt cone, Adv. Aerodyn. **3**, 24 (2021).

[18] C.-L. Chang and M. R. Malik, Oblique-mode breakdown and secondary instability in supersonic boundary layers, J. Fluid Mech. **273**, 323 (1994).

[19] A. C. Laible and H. F. Fasel, Continuously forced transient growth in oblique breakdown for supersonic boundary layers, J. Fluid Mech. **804**, 323 (2016).

[20] X. Chen, S. Dong, G. Tu, X. Yuan, and J. Chen, Boundary layer transition and linear modal instabilities of hypersonic flow over a lifting body, J. Fluid Mech. **938**, A8 (2022).

[21] S. Stanfield, R. Kimmel, D. Adamczak, and T. Juliano, Boundary-layer transition experiment during reentry of HIFiRE-1, J. Spacecr. Rockets **52**, 637 (2015).

[22] S. Schneider, Hypersonic laminar-turbulent transition on circular cones and scramjet forebodies, Prog. Aerosp. Sci. **40**, 1 (2004).

[23] T. Juliano, R. Kimmel, S. Willems, A. Gülhan, and S. Schneider, HIFiRE-1 surface pressure fluctuations from high Reynolds, high angle ground test, in *Proceedings of the 52nd Aerospace Sciences Meeting* (AIAA, Reston, VA, 2014), paper AIAA 2014-0429.

[24] G. Tu, J. Chen, X. Yuan, Q. Yang, M. Duan, Q. Yang, Y. Duan, X. Chen, B. Wan, and X. Xiang, Progress in flight tests of hypersonic boundary layer transition, Acta Mech. Sin. **37**, 1589 (2021).

[25] V. DiCristina, Three-dimensional boundary layer transition on a sharp 8° cone at Mach 10, AIAA J. **8**, 852 (1970).

[26] M. S. Holden, D. Bower, and K. Chadwick, Measurements of boundary layer transition on cones at angle of attack for Mach numbers from 11 to 13, in *Proceedings of the Fluid Dynamics Conference* (AIAA, Reston, VA, 1995), paper AIAA 1995-2294.

[27] P. Yang, Natural transition on the windward side of a hypersonic inclined hypersonic cone at 5 degree angle of attack (in Chinese), in 19th National Conference on Computational Fluid Dynamics, Nanjing, China, 2021 (unpublished).

[28] P. Yang, Z. Tang, J. Chen, X. Yuan, X. Chen, and S. Dong, Temporal evolution of wavepackets on the windward side of an inclined hypersonic cone under a flight condition (in Chinese), Acta Aeronaut. Astronaut. Sin. **42**, 726 (2021).

[29] F. P. Bertolotti, Th. Herbert, and P. R. Spalart, Linear and nonlinear stability of the Blasius boundary layer, J. Fluid Mech. **242**, 441 (1992).

[30] Th. Herbert, Parabolized stability equations, Annu. Rev. Fluid Mech. **29**, 245 (1997).

[31] P. Paredes, A. Hanifi, V. Theofilis, and D. S. Henningson, The nonlinear PSE-3D concept for transition prediction in flows with a single slowly-varying spatial direction, Procedia IUTAM **14**, 36 (2015).

[32] P. Paredes, M. Choudhari, and F. Li, Mechanism for frustum transition over blunt cones at hypersonic speeds, J. Fluid Mech. **894**, A22 (2020).

[33] F. Li, M. Choudhari, C-L Chang, R. Kimmel, D. Adamczak, and M. Smith, Transition analysis for the ascent phase of HIFiRE-1 flight experiment, J. Spacecr. Rockets **52**, 1283 (2015).

[34] T. P. Wadhams, E. Mundy, M. G. MacLean, and M. S. Holden, Ground test studies of the HIFiRE-1 transition experiment, Part 1: Experimental results, J. Spacecr. Rockets **45**, 1134 (2008).

[35] X. Li, D. Fu, and Y. Ma, Direct numerical simulation of boundary layer transition over a blunt cone, AIAA J. **46**, 2899 (2008).

[36] J. Sivasubramanian and H. F. Fasel, Numerical investigation of the development of three-dimensional wavepackets in a sharp cone boundary layer at Mach 6, J. Fluid Mech. **756**, 600 (2014).

[37] J. Sivasubramanian and H. F. Fasel, Direct numerical simulation of transition in a sharp cone boundary layer at Mach 6: fundamental breakdown, J. Fluid Mech. **768**, 175 (2015).

[38] F. Li, M. Choudhari, and P. Paredes, Streak instability analysis for BOLT configuration, in *Proceedings of the AIAA Aviation 2020 Forum* (AIAA, Reston, VA, 2020), paper AIAA 2020-3028.

[39] X. Li, J. Chen, Z. Huang, Q. Yang, and G. Xu, Stability analysis and transition prediction of streamwise vortices over a yawed cone at Mach 6, Phys. Fluids **32**, 124110 (2020).

[40] M. Malik and R. Spall, On the stability of compressible flow past axisymmetric bodies, J. Fluid Mech. **228**, 443 (1991).

[41] M. R. Malik, Numerical methods for hypersonic boundary layer stability, J. Comput. Phys. **86**, 376 (1990).

[42] M. Hermanns and J. A. Hernández, Stable high-order finite-difference methods based on non-uniform grid point distributions, Int. J. Numer. Meth. Fluids **56**, 233 (2008).

[43] Y. Zhu, X. Chen, J. Wu, S. Chen, C. Lee, and M. GadelHak, Aerodynamic heating in transitional hypersonic boundary layers: Role of second-mode instability, Phys. Fluids **30**, 011701 (2018).

[44] L. Ng and G. Erlebacher, Secondary instabilities in compressible boundary layers, Phys. Fluids **4**, 710 (1992).

[45] X. Chen, G. Huang, and C. Lee, Hypersonic boundary layer transition on a concave wall: stationary Görtler vortices, J. Fluid Mech. **865**, 1 (2019).

[46] X. Chen, J. Chen, X. Yuan, G. Tu, and Y. Zhang, From primary instabilities to secondary instabilities in Görtler vortex flows, Adv. Aerodyn. **1**, 19 (2019).

[47] X. Chen, J. Chen, S. Dong, G. Xu, and X. Yuan, Stability analyses of leeward streamwise vortices for a hypersonic yawed cone at 6 degree angle of attack, Acta Aerodyn. Sin. **38**, 299 (2020).

[48] N. De Tullio, P. Paredes, N. D. Sandham, and V. Theofilis, Laminar-turbulent transition induced by a discrete roughness element in a supersonic boundary layer, J. Fluid Mech. **735**, 613 (2013).

[49] Y. Ma and X. Zhong, Receptivity of a supersonic boundary layer over a flat plate. Part 1. wave structures and interactions, J. Fluid Mech. **488**, 31 (2003).

[50] R.-S. Lin and M. R. Malik, On the stability of attachment-line boundary layers. part 1. the incompressible swept hiemenz flow, J. Fluid Mech. **311**, 239 (1996).

[51] M. Choudhari, C.-L. Chang, T. Jentink, F. Li, K. Berger, G. Candler, and R. Kimmel, Transition analysis for the HIFiRE-5 vehicle, in *Proceedings of the 39th AIAA Fluid Dynamics Conference* (AIAA, Reston, VA, 2009), paper AIAA 2009-4056.

[52] Y. Xi, J. Ren, and S. Fu, Hypersonic attachment-line instabilities with large sweep Mach numbers, J. Fluid Mech. **915**, A44 (2021).

[53] P. Paredes, R. Gosse, V. Theofilis, and R. Kimmel, Linear modal instabilities of hypersonic flow over an elliptic cone, J. Fluid Mech. **804**, 442 (2016).

[54] S. P. Schneider, Development of hypersonic quiet tunnels, J. Spacecr. Rockets **45**, 641 (2008).

[55] J. Sivasubramanian and H. F. Fasel, Direct numerical simulation of laminar-turbulent transition in a flared cone boundary layer at Mach 6, in *Proceedings of the 54th AIAA Aerospace Sciences Meeting* (AIAA, Reston, VA, 2016), paper AIAA 2016-0846.

[56] C. Hader and H. F. Fasel, Towards simulating natural transition in hypersonic boundary layers via random inflow disturbances, J. Fluid Mech. **847**, R3 (2018).

[57] F. M. White, *Viscous Fluid Flow* (McGraw-Hill, New York, 2006).

[58] X. Wu, Nonlinear theories for shear flow instabilities: Physical insights and practical implications, Annu. Rev. Fluid Mech. **51**, 451 (2019).

[59] C. Hader and H. F. Fasel, Direct numerical simulation of hypersonic boundary-layer transition for a flared cone: fundamental breakdown, J. Fluid Mech. **869**, 341 (2019).

[60] B. Chu, On the energy transfer to small disturbances in fluid flow (Part I), Acta Mech. **1**, 215 (1965).

[61] S. A. Orszag and A. T. Patera, Secondary instability of wall-bounded shear flows, J. Fluid Mech. **128**, 347 (1983).

[62] M. R. Hajj, R. W. Miksad, and E. J. Powers, Fundamental-subharmonic interaction: Effect of phase relation, J. Fluid Mech. **256**, 403 (1993).

[63] M. T. Landahl, A note on an algebraic instability of inviscid parallel shear flows, J. Fluid Mech. **98**, 243 (1980).

[64] K. M. Butler and B. F. Farrell, Three-dimensional optimal perturbations in viscous shear flow, Phys. Fluids A **4**, 1637 (1992).

[65] X. Chen, L. Wang, and S. Fu, Energy transfer of hypersonic and high-enthalpy boundary layer instabilities and transition, Phys. Rev. Fluids **7**, 033901 (2022).

[66] W. Schoppa and F. Hussain, Coherent structure generation in near-wall turbulence, J. Fluid Mech. **453**, 57 (2002).

[67] C. Hader, N. Deng, and H. F. Fasel, Direct numerical simulations of hypersonic boundary-layer transition for a straight cone at Mach 5, in *Proceedings of the AIAA Scitech 2021 Forum* (AIAA, Reston, VA, 2021), paper AIAA 2021-0743.